# THREE DIMENSIONAL CONTROLLED-SOURCE ELECTROMAGNETIC EDGE-BASED FINITE ELEMENT MODELING OF CONDUCTIVE AND PERMEABLE HETEROGENEITIES

A Dissertation

by

SOUVIK MUKHERJEE

Submitted to the Office of Graduate Studies of
Texas A&M University
in partial fulfillment of the requirements for the degree of

DOCTOR OF PHILOSOPHY

August 2010

Major Subject: Geophysics

# THREE DIMENSIONAL CONTROLLED-SOURCE ELECTROMAGNETIC EDGE-BASED FINITE ELEMENT MODELING OF CONDUCTIVE AND PERMEABLE HETEROGENEITIES

A Dissertation

by

SOUVIK MUKHERJEE

Submitted to the Office of Graduate Studies of
Texas A&M University
in partial fulfillment of the requirements for the degree of

DOCTOR OF PHILOSOPHY

Approved by:

| | |
|---|---|
| Chair of Committee, | Mark Everett |
| Committee Members, | Richard Gibson |
| | Luc Ikelle |
| | Cam Nguyen |
| | Jakub Velimsky |
| Head of the Department, | Andreas Kronenberg |

August 2010

## ABSTRACT

Three Dimensional Controlled-source Electromagnetic Edge-based Finite Element Modeling of Conductive and Permeable Heterogeneities.

(August 2010)

Souvik Mukherjee, BSc., University of Calcutta;

MSc., Jadavpur University;

M.Tech, Indian Institute of Technology, Kharagpur;

M.S., University of Utah

Chair of Advisory Committee: Dr. Mark E. Everett

Presence of cultural refuse has long posed a serious challenge to meaningful geological interpretation of near surface controlled–source electromagnetic data (CSEM). Cultural refuse, such as buried pipes, underground storage tanks, unexploded ordnance, is often highly conductive and magnetically permeable. Interpretation of the CSEM response in the presence of cultural noise requires an understanding of electromagnetic field diffusion and the effects of anomalous highly conductive and permeable structures embedded in geologic media. While many numerical techniques have been used to evaluate the response of three dimensional subsurface conductivity distributions, there is a lack of approaches for modeling the EM response incorporating variations in both subsurface conductivity $\sigma$ and relative permeability $\mu_r$.

In this dissertation, I present a new three dimensional edge–based finite element (FE) algorithm capable of modeling the CSEM response of buried conductive and

permeable targets. A coupled potential formulation for variable $\mu$ using the vector magnetic potential $\boldsymbol{A}$ and scalar electric potential $V$ gives rise to an ungauged curl–curl equation. Using reluctivity ($\upsilon=1/\mu$), a new term in geophysical applications instead of traditional magnetic susceptibility, facilitates a separation of primary and secondary potentials. The resulting differential equation is solved using the finite element method (FEM) on a tetrahedral mesh with local refinement capabilities. The secondary $\boldsymbol{A}$ and $V$ potentials are expressed in terms of the vector edge basis vectors and the scalar nodal basis functions respectively. The finite element matrix is solved using a Jacobi preconditioned QMR solver. Post processing steps to interpolate the vector potentials on the nodes of the mesh are described. The algorithm is validated against a number of analytic and multi dimensional numeric solutions. The code has been deployed to estimate the influence of magnetic permeability on the mutual coupling between multiple geological and cultural targets. Some limitations of the code with regards to speed and performance at high frequency, conductivity and permeability values have been noted. Directions for further improvement and expanding the range of applicability have been proposed.

## ACKNOWLEDGMENTS

First of all I would like to thank my advisor, Dr. Mark Everett, for devoting countless weekends, holidays, and late evening hours to finally make this dissertation a reality. Thank you for providing critical suggestions, tips, references, insights and actually getting your hands dirty with the code. Thank you for also enhancing my knowledge of hops significantly.

I would like to thank my committee members, Dr. Luc Ikelle, Dr. Jakub Velimsky, Dr. Rick Gibson, and Dr. Cam Nguyen, for always being there to help and provide general guidance, not to mention helping meet all the document deadlines. Also special thanks to Dr. Jakub Velimsky for providing me his thesis and helping me navigate the tricky and often murky waters of reference tetrahedron, inner products, and analytic evaluation of triple integrals.

I would like to thank Yoonho Song of Korea Institute of Geoscience and Mineral Resources (KIGAM) for making available the data from his 2.5–D code for comparison when many others were either too busy or reluctant.

I would like to thank my wife, Shikha Khatri, for persevering through six years and one degree of separation. Thanks to our parents: thank you for everything. Your contributions and sacrifices towards making this day happen would fill pages of another dissertation.

Special thanks to Mrs. Elaine Everett. Thanks for too many things to list here, but your support in this entire process was absolutely indispensable.

Thanks to all my colleagues: Roland Fernandes, Douglas Sassen, Carl Pierce, Alfonso Benavides, Suwimon Udphuay, David Dickins, Katie Decker, and Mark Hickey.

Thanks to Drs. Chris Harris of Shell and Rick Rosthal of EMI Schlumberger for being stellar mentors during my internship in your teams; they have shaped and furthered my understanding of both CSEM and the FEM by many a mile.

Finally, thanks to all my colleagues in Shell, especially my team lead, Gary Scott Steffens, and discipline chief, Denise Butler, for the absolutely critical and indispensable support that they have provided these last two years.

## TABLE OF CONTENTS

Page

Page

## LIST OF FIGURES

Page

Page

Page

## LIST OF TABLES

Page

# 1. INTRODUCTION

The controlled source electromagnetic (CSEM) method is an important technique in geophysical exploration with an increasing range of applications. The CSEM method employs an electromagnetic transmitter that is energized by a transient or time–harmonic current, while the response generated by the subsurface is measured at specified receiver locations. CSEM is an increasingly popular method in the oil and gas industry (Constable, 2006), and has long been an essential geophysical technique in the mining industry (Grant and West, 1965). The technique is also used in various near surface applications such as mapping permafrost, groundwater exploration, environmental site characterization, UXO remediation, geotechnical assessment, and archaeological prospecting (eg. Palacky, 1988; Buselli et al. 1990; Edwards et al. 1988; Hoekstra and Blohm, 1990; Senos Matias et al. 1994; Everett and Meju, 2005).

The behavior of electromagnetic fields is governed by three properties of the subsurface (Grant and West, 1965) : electrical conductivity $\sigma$; magnetic permeability $\mu$; and dielectric permittivity $\varepsilon$. Most geologic materials are non–magnetic, i.e. $\mu = \mu_o$ (the free space permeability). At low frequencies ($\omega << \sigma/\varepsilon$, where $\omega$ is the angular frequency), Maxwell's equations are simplified to their magnetoquasistatic limit (Larsson, 2007), and displacement currents may be neglected.

---

This dissertation follows the journal style of Geophysics.

This results in diffusive governing equations, and the response is most importantly a function of the distribution of the subsurface conductivity. The latter, in turn, is diagnostic of spatial variations in geology, such as lithologic and structural boundaries, and the distribution of fluids. A recent surge of interest in environmental problems has opened new avenues of application for the controlled–source electromagnetic method (CSEM). The presence of man–made debris, such as buried pipes, drums, unexploded ordnance (UXO) and other steel objects, introduces significant complexity to the CSEM response. This cultural noise, in addition to having high conductivity, oftentimes has significant relative magnetic permeability ($\mu_r = \mu/\mu_o$) (Eskola et al, 1999).

Interpretation of the CSEM response in the presence of cultural noise requires an understanding of electromagnetic field diffusion and the effects of anomalous highly conductive and permeable structures (hereinafter called targets) embedded in geologic media. A geologic medium is often modeled as a sequence of layers of different conductivity (eg. Ryu et al. 1970); a more realistic model is two and a half dimensional (2.5–D) (eg. Everett and Edwards, 1993), in which the subsurface consists of spatially varying geology characterized by an invariant two dimensional cross section of infinite strike length, excited by a 3–D electromagnetic source. Another widely–used approximation of a geologic medium is a thin sheet in free space or buried in a homogeneous or layered Earth. The electromagnetic response of a thin conductive sheet (Price, 1949) is of considerable interest in exploration geophysics. The method has been widely used in the mining industry as an effective approximation for modeling

conductive ore bodies of large areal extent but limited thickness (eg. Pavlov and Zhdanov, 2001) buried within a resistive host medium. The thin sheet model simplifies the physics of electromagnetic induction in three dimensional structures (Annan, 1974; Walker and West, 1992) yet provides a good approximation to the geometry of elongated tabular bodies. Realistically, all geologic bodies have finite length extent in all three dimensions. Though assumptions of infinite strike length work well in a number of scenarios, e.g. mid oceanic ridges (Everett and Edwards, 1993), increasing computational capabilities and advances in numerical modeling techniques now permit accurate modeling of CSEM field responses of bodies of arbitrary geometry and finite spatial extent. Three dimensional modeling of the response of geologic structures to controlled–source electromagnetic (CSEM) excitation has been explored in a number of recent papers (Lee et al.,1981; Xiong, 1992; Newman and Alumbaugh, 1995; Sugeng, 1998; Aruliah et al.,1999; Hursan and Zhdanov, 2002; Weiss and Newman, 2002; Stalnaker, 2004).

Many numerical techniques have been used to evaluate the response of three dimensional subsurface conductivity distributions, including integral equation (e.g. Raiche and Coggon, 1974; Hohmann, 1987; Xiong and Tripp, 1995; Aruliah et al. 1999), finite difference (e.g. La Brecque, 1995; Newman and Alumbaugh, 1995), finite element (e.g. Everett and Schultz, 1996; Sugeng, 1998; Badea et al. 2001), and hybrids of such methods (e.g. Lee et al. 1981). While substantial progress has been achieved in terms of accuracy and computational efficiency in modeling the subsurface conductivity, there is a lack of approaches for modeling the EM response incorporating variations in both

subsurface conductivity and permeability. The near surface CSEM response is significantly influenced by the presence of permeable ($\mu_r > 1$) targets of both anthropogenic and geologic origin (eg. Szarka, 1988). It is thus important to understand the effects of permeability on the CSEM response of three dimensional targets for more accurate interpretation of CSEM data. The response of a conducting and permeable sphere in free space due to a time varying magnetic dipole has been calculated by Grant and West (1965) in the frequency domain and by Nabighian (1971) in the time domain. Since then, there have been a few additional analytic solutions (eg. Rai and Verma, 1982; Batayneh, 2001), but numerical modeling of isolated three dimensional targets embedded within an inhomogeneous geological host is rarely found in the geophysical literature.

**1.1 The relative contribution of current modes to the CSEM response**

The CSEM response of a nonmagnetic ($\mu_r = 1$) conductive body located in a conductive host can be decomposed into two modes of excitation : the inductive mode, in which the induced electric current is confined to circulate inside the conductor, and the galvanic, or current channeling mode in which electric current gathered from the host medium flows through the conductor (e.g. Lamontagne and West, 1971; Annan, 1974; Walker and West, 1991 and 1992). The relative strength of the inductive and galvanic modes in a thin sheet can be estimated in terms of a "current excitation ratio" (Walker and West , 1992) consisting of two factors : 1) a simple product of the conductivity, frequency, and the dimension of the plate providing a measure of the relative "saturation" of galvanic and inductive modes ; and 2) the local ratio of the electric and

magnetic fields described as a "local impedance" (Walker and West, 1992). Accordingly, for a thin square sheet of side $a$, conductivity $\sigma_a$, excited at angular frequency $\omega$, the induction number $K$ is given by (Walker and West, 1992)

$$K = \mu_0 \frac{\omega \sigma_a a}{8}. \tag{1}$$

On the other hand, the channeling number $C$ is a measure of galvanic mode saturation (Walker and West, 1992)

$$C = \frac{\sigma_a}{2\sigma_b a}; \tag{2}$$

where, $\sigma_b$ is the background conductivity. If $K < 1$, the conductor is inductively unsaturated while if $C < 1$ then the conductor is galvanically unsaturated. When both $K \sim 1$and $C \sim 1$, the conductor is excited by a mixture of the modes. The relative contribution from the source to each mode of current excitation in a given conductor depends on the ratio of the incident electric $E$- and magnetic $H$- field intensities, as characterized by a "local impedance"(Walker and West, 1992) :

$$Z = \frac{E}{H} = \sqrt{\frac{\omega \mu_0}{\sigma_b}} 10^r; \tag{3}$$

where $r$ is a spatially dependent geometric factor associated with the source. A knowledge of the relative strengths of the two modes of current excitation in different elements of a conductive earth model provides improved understanding of the interaction between geophysical targets and host geology. This understanding in turn, can help in isolating or accounting for the effects of "known" contributors to the

electromagnetic signal at a geophysical site. Examples of such contributors include buried powerlines, scattered cultural debris, underground storage tanks, etc (e.g. Qian and Boerner, 1994; Stalnaker et al. 2006; Fernandes, 2008).

In magnetic ($\mu_r > 1$) bodies, a third mode is present: the magnetization mode. This is the field due to magnetic moment $\boldsymbol{m}$ of a magnetic dipole and is given as (Jackson, 1975)

$$\boldsymbol{B}(\boldsymbol{r}) = \frac{3(\boldsymbol{m}.\boldsymbol{r})\boldsymbol{r} - \boldsymbol{m}}{|\boldsymbol{r}|^3}. \tag{4a}$$

It is also well known (eg. Ulaby, 2004) that equation (4*a*) is simplified for the field component $H_z$ due to a *z*- directed magnetic dipole of magnetic moment $m_z$

$$H_z = \frac{m_z}{2\pi r^3}. \tag{4b}$$

The measured CSEM response, which is proportional to the magnetic fields $B_z$ or $H_z$, is a function of the contribution from the above modes. The variation in $\sigma_a$, and $\mu_r$ of a geophysical target can lead to different levels of excitation of the three different modes. The chief contributor to the magnetization mode is the strength of the magnetic moment $\boldsymbol{m}$ which in turn is dependent on the relative permeability $\mu_r$. Thus, a key role of $\mu_r$ in electromagnetic induction is to increase the contribution from magnetization mode to the secondary field of the target.

While the present analysis is primarily concerned with the CSEM response in the frequency domain, it is instructive to look at the fundamental time constant of a spherical body excited by a transient magnetic dipole (Pasion, 2007). The fundamental time

constant, $\tau_0$ determines the onset of late time exponential decay behavior of the secondary magnetic field of the sphere. For a non permeable ($\mu_r = 1$) sphere of conductivity $\sigma$, and radius $a$, this is given by

$$\tau_0(\mu_r = 1) = \frac{\sigma\mu_0 a^2}{\pi^2}. \tag{5a}$$

For a permeable ($\mu_r > 1$) sphere the fundamental time constant is expressed as

$$\tau_0 = \frac{\sigma\mu_0\mu_r a^2}{q_1^2}; \tag{5b}$$

where $q_1$ is a root of the transcendental equation

$$\tan q_1 = \frac{(\mu_r - 1)q_1}{q_1^2 + (\mu_r - 1)}; \tag{6}$$

Pasion (2007) shows that the value of $q_1$ lies between $\pi$ ($\mu_r = 1$) and 4.4934 ($\mu_r = \infty$). It is evident from equations (5*a*) and (5*b*) that the decay constant for the non magnetic eddy – current mode is different from that of the magnetization mode and the contribution to the secondary magnetic field response of the latter is not a matter of simply scaling equation (5*a*) by $\mu_r$.

Figure 1 illustrates this point. The analytic solution of the secondary $H_z$ field of a conducting, permeable sphere excited by an oscillating dipole in free space is computed using the solution in Rai and Verma (1982). The product $\sigma_a\mu_r$ = 12000 S/m in each case. The response for various oscillation frequencies of the dipole are plotted at the dipole location. The differences in response for the two spheres confirm that the effect of conductivity generating the inductive mode is different from the effect of permeability

generating the magnetization mode in determining the electromagnetic response of the sphere.

Also of particular interest is the peak of the quadrature response at specific frequencies for different values of $\mu_r$ as shown in Figure 2. As $\mu_r$ increases from 1 to 5, the peak quadrature response shifts to lower frequency. This is an important result for understanding the relative contributions of the inductive mode of current excitation, and the magnetization mode to the secondary magnetic field of the sphere. Since this is a single isolated sphere in free space, it has no current channeling mode.

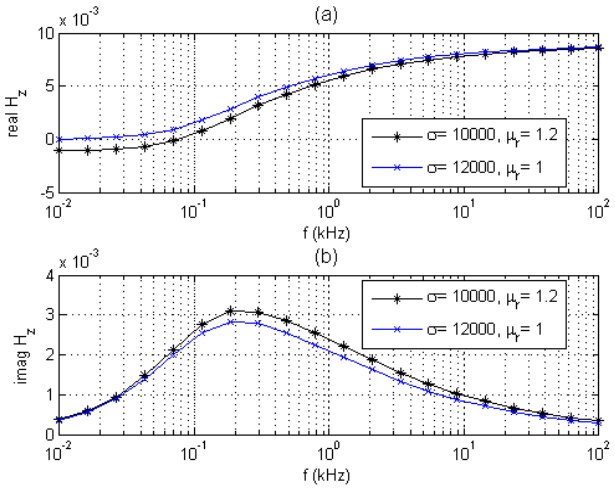


**Figure 1.** Secondary $H_z$ response of a sphere of 0.9m radius, placed 2.0 m under an oscillating magnetic dipole in free space. Conductivity of the sphere is $\sigma_a$ =$10^4$S/m and $\mu_r$ = 1.2 for the black curve and $\sigma_a$ =12000 S/m and $\mu_r$ =1.0 for the blue curve. Thus, the product $\sigma_a\mu_r$ is the same for both models. The response is calculated at the dipole location for a range of frequencies. (*a*) The real part of secondary $H_z$ (A/m). (*b*) The imaginary part of secondary $H_z$ (A/m).

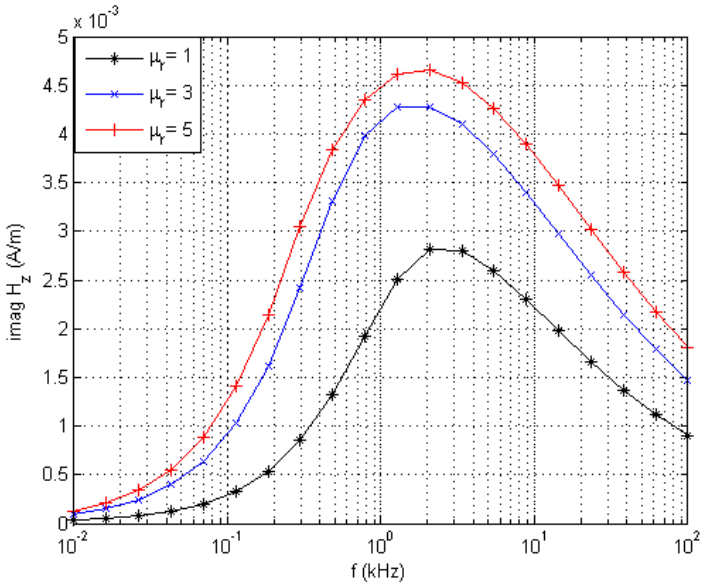


**Figure 2.** Quadrature of secondary $H_z$ response of a sphere of 0.9m radius, placed 2.0 m under an oscillating magnetic dipole in free space. Conductivity of the sphere is $\sigma_a$ =$10^4$S/m and $\mu_r$ = 1.0 for the black curve, $\mu_r$ = 3.0 for the blue curve, and $\mu_r$ =5.0 for the red curve. The response is calculated at the dipole location for a range of frequencies.

### 1.2 Literature review

Forward modeling of the EM induction problem ideally satisfies three main criteria:

(*a*) capability to model arbitrary target geometries; (*b*) capability to model high conductivity contrasts between host geology and target, and; (*c*) high computational efficiency. Criterion (c) makes the volume integral method (Xiong, 1992) and its approximations (e.g. Habashy et al, 1993, Zhdanov and Tartaras, 2002) very attractive for rapidly solving geophysical exploration problems. These methods require only the local heterogeneous domain of interest to be discretized. However, numerical

experiments (Raiche et al. 2003) suggest that volume integral methods are limited to a maximum conductivity contrast of 300:1. For various IE approximations (Zhdanov and Fang, 1997; Zhdanov and Tartaras, 2002) this contrast is lowered to less than 30:1. Finite difference methods (FDM), can model high contrasts of around $10^5$:1 (Newman and Alumbaugh, 1995), but lack sufficient geometric flexibility to model complex shapes: for example, FD meshes are rectilinear and produce "staircase" type approximations of dipping structures. Finite element methods (FEM) provide both geometric flexibility and the capability to model high contrasts of greater than $10^5$ : 1 (Sugeng and Raiche, 2004; Stalnaker et al. 2006). Coggon (1971) was the first to demonstrate the applicability of FEM to geophysical electromagnetic (EM) problems. Since then, there have been many advances in accuracy, flexibility, and computational efficiency. These advances have focused on five broad areas: (*a*) choice of variable in the differential equation, i.e. fields or potentials; (*b*) choice of basis functions, i.e. nodal scalar or edge vector; (*c*) choice of linear system solver, i.e. direct or iterative; (*d*) the post processing steps, which include converting potentials to fields, computing magnetic from electric fields, or converting edge values of fields and potentials to nodal values, and; (*e*) mesh generation capabilities including local refinement and conformance to curved structures such as spheroids.

An interesting approach is to model a three dimensional source exciting two dimensional structure – traditionally known as the 2.5 –D approach. Many geologic structures such as angular unconformities, dikes, dipping beds, and fault zones, can be adequately represented as idealized 2–D structures with respect to conductivity

variations, while a 3–D source provides a realistic description of the excitation. The 2.5–D approach serves as an effective compromise in FEM modeling of electromagnetic problems in geophysics (Everett and Edwards, 1993; Unsworth et al. 1993) since limited computational power is required. The early 2.5–D approaches were formulated in terms of electric and magnetic fields directly. The relatively small size of the coefficient (stiffness) matrix renders the method amenable to stable solutions without raising any serious issues regarding the condition number of the matrix. However, when transitioning to the full 3–D problem, the increase of the matrix size (~ O ($n^2$) to an O ($n^3$) ) can lead to a poorly conditioned matrix at high contrasts unless a suitable penalty functional is used (Zunoubi et al. 1999). Everett and Schultz (1996) introduced a Coulomb – Gauged coupled $\boldsymbol{A}$-$\psi$ vector magnetic and scalar electric potential formulation for the 3–D geomagnetic induction problem. Aruliah et al. (1999) applied it to the 3–D CSEM problem using integral equations and reported a significantly better conditioned matrix. Badea et al. (2001) applied the coupled potential formulation in the Coulomb–Gauge using an FE formulation following an approach suggested by Biro and Preiss (1989). Using an efficient sparse matrix storage scheme and a powerful iterative QMR solver, storage and computational time requirements are reduced to a manageable level. Conductivity contrasts upto $10^6$:1 are possible using local mesh refinement (Liu and Joe, 1996) for the borehole logging problems considered. Stalnaker et al. (2006) modified the approach of Badea et al. (2001) to calculate the subsurface response due to a current loop source placed on the surface.

### 1.3 Objectives of this study

The primary objective of this study is to develop a three dimensional numerical modeling method to compute the CSEM response of conductive and permeable heterogeneities in geologic media. A finite element method using vector edge basis functions has been developed and tested.

A finite element (FE) method using vector edge basis functions is employed to solve the governing diffusive differential equations. A coupled potential formulation for variable $\mu$ gives rise to an ungauged "curl – curl" equation. Applying traditional FE techniques using nodal basis functions, leads in this case to a poorly conditioned coefficient (stiffness) matrix (Biro, 1999). The edge basis vectors (Sugeng, 1998) provide improved matrix conditioning and a better representation of tangential boundary conditions across material discontinuities (Silvester and Ferrari, 1996). The code has been compared and validated against analytic and multi–dimensional numerical solutions. To demonstrate the applicability of the code to practical geophysical problems I have used it to quantify the effects of mutual interaction between geophysical targets when excited by a CSEM source. Special emphasis has been put on the effects of increased magnetic permeability of targets. This approach can be used to analyze and isolate the effects of "known" cultural noise in the interpretation of CSEM data.

Section 2 of this work presents the EM induction problem as a coupled system of differential equations in terms of secondary potentials. The known primary potentials are those generated in a simple, homogeneous half space due to a current loop oscillating at a specific frequency. I introduce a new term in geophysical applications : reluctivity

($\upsilon=1/\mu$) which simplifies the analysis of permeable, conductive heterogeneities in the subsurface.

Section 3 introduces the edge – based finite element technique for solving the coupled system of differential equations. I use the weak formulation and discretize the solution domain using a tetrahedral mesh allowing local refinement according to the scheme of Liu and Joe (1996) as implemented in Stalnaker (2004). Homogeneous Dirichlet boundary conditions are applied at the outer mesh boundaries.

In Section 4, I validate the results from the code against a series of analytic and numeric solutions and analyze code performance.

In Section 5, I apply the code for estimating the mutual coupling between geophysical targets and their surroundings. Special emphasis is put on the effects of magnetic permeability on the mutual coupling.

Section 6 consists of the conclusions. This includes a summarization of the results and their implications in near surface geophysical exploration. I also explore and explain the limitations of the code. Also, I include recommendations for future applications and development of the code.

# 2. CSEM INDUCTION IN CONDUCTIVE PERMEABLE EARTH

## 2.1 Introduction

A typical CSEM loop–loop survey involves placing the transmitter current loop on or above the ground surface and receiver loop or loops on the surface in various orientations and locations around the transmitter. The problem, in the absence of significant topography, can be modeled with a double half space consisting of an upper half space being the uniform, weakly conducting air region and the lower half space, the heterogeneous conducting earth region. As discussed in the review of existing literature, the diffusive differential equations for the magnetoquasistatic formulation yield a better conditioned matrix for numerical solution when formulated in terms of vector magnetic and scalar electric potentials. The ungauged "curl curl" formulation allows for easy separation of primary and secondary potentials when both conductive and permeable heterogeneities are considered.

## 2.2 The ungauged potential problem for conductive, permeable heterogeneities

Consider an upper half space $\Omega_n$ with boundaries $\Gamma_n$, and a lower conducting region, $\Omega_c$ with boundaries $\Gamma_c$. The interface is defined as $\Gamma_{nc}$ (Figure 3). A transmitter loop of radius *a*, current strength *I*, and angular frequency $\omega$, is placed at height *h* above the ground ($z = 0$). Representing the magnetic field $\boldsymbol{B}$ and the electric field $\boldsymbol{E}$– in terms of a vector magnetic potential $\boldsymbol{A}$ and a scalar electric potential *V*, we have

$$\boldsymbol{B} = \nabla \times \boldsymbol{A};$$

(7a)

$$\boldsymbol{E} = -\left(i\omega\boldsymbol{A} + \nabla V\right).$$

(7b)

Following Badea et al.(2001), explicit modeling of the source is avoided by defining a set of primary potentials ($\boldsymbol{A}_p$, $V_p$) to be the response of a prescribed background model, usually a homogeneous or layered earth. The primary potentials are typically chosen to have an analytic or semi–analytic solution. We can thus define,

$$\boldsymbol{A} = \boldsymbol{A}_p + \boldsymbol{A}_s; \tag{8a}$$

$$V = V_p + V_s. \tag{8b}$$

Here, the subscript *p* denotes a primary potential and *s* denotes a secondary potential. Similarly, the conductivity ($\sigma$), permeability ($\mu$), and reluctivity ($\upsilon$) may be decomposed into primary and secondary parts,

$$\sigma = \sigma_p + \sigma_s; \tag{9a}$$

$$\mu = \mu_p + \mu_s; \tag{9b}$$

$$1/\mu = \upsilon = \upsilon_p + \upsilon_s; \tag{9c}$$

and

$$\upsilon_p = 1/\mu_p. \tag{9d}$$

It must be noted here that

$\upsilon_s \neq 1/\mu_s$ , but rather

$$\upsilon_s \equiv \upsilon - \upsilon_p = \frac{1}{\mu_p + \mu_s} - \frac{1}{\mu_p} = \frac{-\mu_s}{\mu_p(\mu_p + \mu_s)}. \tag{9e}$$

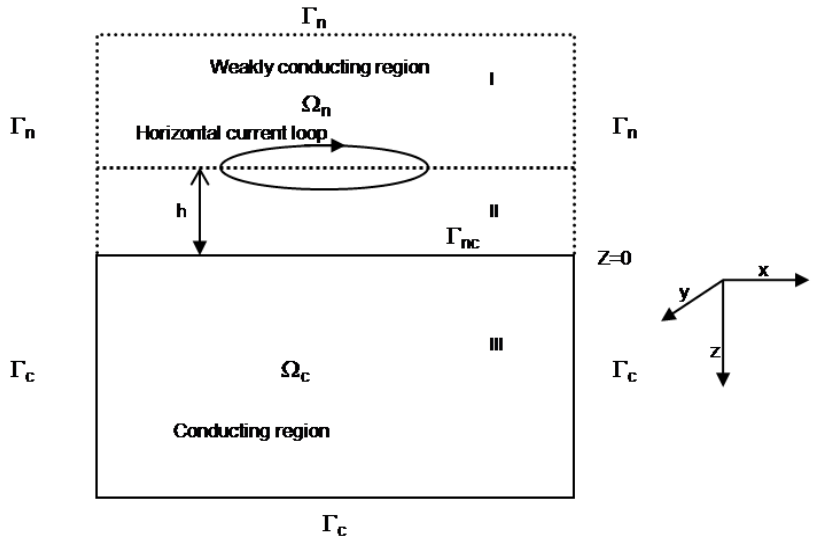


**Figure 3.** A schematic representation of the earth model excited by an electromagnetic loop source.

As shall be seen subsequently, reluctivity $\upsilon$ is preferred to permeability $\mu$ in the governing equations since it facilitates the separation of primary and secondary potentials (Biro, 1999).

Now, from Maxwell's equations, the total potentials $(\boldsymbol{A}, V)$ satisfy

$$\nabla \times (\upsilon \nabla \times \boldsymbol{A}) + i\omega\sigma\boldsymbol{A} + \sigma\nabla V = 0; \tag{10a}$$

If $\sigma = \sigma_p$ and $\upsilon = \upsilon_p$, the solution to equation (10*a*) is denoted as $\boldsymbol{A}_p$ and $V_p$, satisfying

$$\nabla \times (\upsilon_p \nabla \times \boldsymbol{A}_p) + i\omega\sigma_p\boldsymbol{A}_p + \sigma_p\nabla V_p = 0. \tag{10b}$$

The secondary potentials ($\boldsymbol{A}_s$ , $V_s$ ) are readily shown to satisfy

$$\nabla\times\left(\upsilon\nabla\times\boldsymbol{A}_s\right)+i\omega\sigma\boldsymbol{A}_s+\sigma\nabla V_s=-\nabla\times\left(\upsilon_s\nabla\times\boldsymbol{A}_p\right)-\sigma_s\nabla V_p-i\omega\sigma_s\boldsymbol{A}_p; \tag{11}$$

The choice of formulating the CSEM forward problem in terms of reluctivity $\upsilon$, is thus an important one: it allows us to organize the governing equations with the unknown secondary potentials ($\boldsymbol{A}_s$,$V_s$) on the left side and the known primary potentials ($\boldsymbol{A}_p$,$V_p$ ) acting as the source terms on the right side. This organization is not possible in terms of permeability, $\mu = \mu_p + \mu_s$. The potentials ($\boldsymbol{A}$, $V$ ) represent four unknown scalar functions, while equation (11) is just a 3 – component vector equation. An additional scalar equation is needed to close the system.

In the magnetoquasistatic formulation (Larsson, 2007), the current density, $\boldsymbol{J}=\sigma\boldsymbol{E}$, is divergence – free, leading to

$$\begin{aligned}&\nabla\cdot\boldsymbol{J}=0;\\&\Rightarrow\nabla\cdot\left(\sigma\boldsymbol{E}\right)=0.\end{aligned} \tag{12}$$

Using equation (7*b*) in (12), we have

$$-\nabla\cdot\left(i\omega\sigma\boldsymbol{A}+\sigma\nabla V\right)=0. \tag{13a}$$

As before, the primary potentials

$$-\nabla\cdot\left(i\omega\sigma_p\boldsymbol{A}_p+\sigma_p\nabla V_p\right)=0. \tag{13b}$$

Equation (13a) can then be organized as

$$-\nabla\cdot\left(i\omega\sigma\boldsymbol{A}_s+\sigma\nabla V_s\right)=\nabla\cdot\left(i\omega\sigma_s\boldsymbol{A}_p+\sigma_s\nabla V_p\right); \tag{14}$$

which is the scalar equation that closes the system.

Equations (11) and (14) constitute a coupled system of PDEs in terms of the unknown secondary potentials ($\boldsymbol{A}_s, V_s$) with excitation provided by the known primary potentials ($\boldsymbol{A}_p, V_p$ ). In the next section, we shall solve this system of equations using an edge based FEM technique.

# 3. APPLYING FEM TO THE CSEM UNGAUGED COUPLED POTENTIAL PROBLEM

## 3.1 The weak formulation using mixed node and edge elements

In Section 2, I have defined the CSEM induction problem as an ungauged coupled potential system of PDEs (equations 11 and 14). In order to solve this system of equations, I discretize the domain $\Omega=\Omega_n \cup \Omega_c$ (Figure 3 in Section 2) using a rectilinear mesh (Stalnaker, 2004) with tetrahedral elements and capability for local mesh refinement as described by Liu and Joe (1996) and implemented in Badea et al (2001). The material properties, $\mu$ and $\sigma$, are assumed to be constant within each tetrahedron.

I use scalar nodal basis functions to describe the secondary scalar electric potential $V_s$ and vector edge basis functions to describe the secondary magnetic vector potential $\boldsymbol{A}_s$. Accordingly, $V_s$ is expressed as

$$V_s(\boldsymbol{r}) = \sum_{k=1}^{N} b_k \psi_k(\boldsymbol{r}); \tag{15a}$$

where $b_k$ are unknown scalar coefficients, $\psi_k$ are scalar nodal basis functions (Silvester and Ferrari, 1996) and $N$ is the number of nodes in the mesh. Similarly, $\boldsymbol{A}_s$ is expressed as

$$\boldsymbol{A}_s(\boldsymbol{r}) = \sum_{i=1}^{M} a_i \boldsymbol{\alpha}_i(\boldsymbol{r}); \tag{15b}$$

where $a_i$ are unknown scalar coefficients $\boldsymbol{\alpha}_i$ are vector edge basis functions (Silvester and Ferrari, 1996) and $M$ is the number of edges in the mesh. The edge basis functions are linear combinations of nodal basis functions and their gradients;

$$\boldsymbol{\alpha}_i(\boldsymbol{r}) = \psi_b \nabla \psi_a \; - \; \psi_a \nabla \psi_b . \tag{15c}$$

In equation (15c), the indices (*a,b)* refer to the two end nodes of the edge *i*. As implied in equation (15c), the value of the edge basis function $\boldsymbol{\alpha}_i(\boldsymbol{r})$ for an edge (*a,b*) is governed by the values of the nodal basis functions $\psi_a(\boldsymbol{r})$ and $\psi_b(\boldsymbol{r})$ and their gradients. For a given tetrahedron with nodes (*a*, *b*, *c*, *d*), the nodal basis function $\psi_a(\boldsymbol{r})$ is defined on and inside the tetrahedron as (Silvester and Ferrari, 1996),

$$\psi_a(\boldsymbol{r}) = 1 \big|_{\boldsymbol{r}=\boldsymbol{r}(a)}; \tag{16a}$$

$$\psi_a(\boldsymbol{r}) = 0 \big|_{\boldsymbol{r}=\boldsymbol{r}(b),\boldsymbol{r}=\boldsymbol{r}(c),\boldsymbol{r}=\boldsymbol{r}(d)} \tag{16b}$$

$$0 < \psi_a(\boldsymbol{r}) < 1 \big|_{\boldsymbol{r}\neq\boldsymbol{r}(b),\boldsymbol{r}\neq\boldsymbol{r}(c),\boldsymbol{r}\neq\boldsymbol{r}(d)} \tag{16c}$$

The choice of expressing the vector magnetic potential $\boldsymbol{A}$ in terms of the edge basis vectors is an important one : it naturally enforces the continuity conditions of the normal $\boldsymbol{B}$– and the tangential $\boldsymbol{E}$ – fields across the material interface between two tetrahedron which may have different material properties ($\sigma$, $\mu$). As shown in Figure 4, let the common face (triangle) $\tau$ between two connected tetrahedra (1 & 2) be shared by nodes *a, b*, and *c*. Following Silvester and Ferrari (1996), the gradient of a nodal basis function defined by vertex *d* of tetrahedron 1 is perpendicular (normal) to the opposing face. Thus, the tangential component $A_{tan}$ of vector potential $\boldsymbol{A}$ on $\tau$ is essentially a function of edges *p*, *q*, and *r* belonging to the triangle $\tau$ as evident from equation (15*c*). Since the edges *p*, *q*, and *r* are common to both tetrahedra 1 and 2, it follows $A_{tan}$ is continuous on

the interface $\tau$ between tetrahedra 1 and 2. The curl of $A_{tan}$ is normal to itself and from equation (7*a*), can be expressed as the normal component of $\boldsymbol{B}$ –, $B_{normal}$. Thus, if $A_{tan}$ is continuous, $B_{normal}$ is also continuous. Also, from equations (7*b*), (15*a*), and (15*b*) it can be shown that the tangential $\boldsymbol{E}$ – field, $E_{tan}$ is coplanar with and a function of $A_{tan}$. Thus, if $A_{tan}$ is continuous then $E_{tan}$ must also be continuous on $\tau$. Thus, the continuity conditions of the fields are naturally enforced by representing $\boldsymbol{A}$ in terms of the edge basis vectors. It is also instructive to look at the behavior of the component of the $\boldsymbol{E}$ – field normal to the common interface, $\tau$. Once again, from equations (7*b*), (15*a*), and (15*b*), it can be shown that the $E_{normal}$ component in tetrahedra 1 is parallel to the gradient of the nodal basis function associated with node *d* and parallel to the gradient of node *e* in tetrahedra 2. As defined in Silvester and Ferrari (1996), these gradient vectors are constant and defined only within a given tetrahedron. Two different nodes in two different tetrahedra will have different gradients. This implies that the $E_{normal}$ component is discontinuous across the interface $\tau$, which is a natural discontinuity relation across material discontinuities. A similar argument may be made about the discontinuity of the tangential $\boldsymbol{B}$ – field, noting that it is derived from the curl of the normal component of the vector magnetic potential $\boldsymbol{A}$, which is discontinuous. Thus both continuity and discontinuity relations of the field components are naturally enforced by defining the vector magnetic potential in terms of the edge basis vectors.

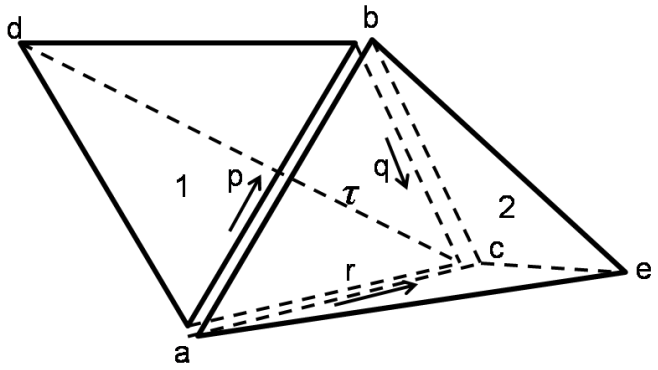


**Figure 4.** A pair of connected tetrahedra (modified from Silvester and Ferrari, 1996). The common face is the triangle, $\tau$ defined by common nodes *a*, *b*, and *c*, and the common edges *p*, *q*, and *r*. By choosing the edge basis functions to define the vector magnetic potential, the continuity conditions of the tangential $\boldsymbol{E}$– and normal $\boldsymbol{B}$– fields are naturally enforced.

Using $\boldsymbol{\alpha}_j$ as the test functions to establish the weak formulation for (11), we have,

$$\left(\boldsymbol{\alpha}_j, \nabla\times\upsilon\nabla\times\sum_{i=1}^{M} a_i\boldsymbol{\alpha}_i\right)+\left(\boldsymbol{\alpha}_j, i\omega\sigma\sum_{i=1}^{M} a_i\boldsymbol{\alpha}_i\right)+\left(\boldsymbol{\alpha}_j, \sigma\nabla\sum_{k=1}^{N} b_k\psi_k^c\right)=-\left(\boldsymbol{\alpha}_j, \begin{bmatrix}\nabla\times\left(\upsilon_s\nabla\times\boldsymbol{A}_p\right)+..\\ .\sigma_s\left(\nabla V_p+i\omega\boldsymbol{A}_p\right)\end{bmatrix}\right). \tag{17}$$

Here $(u,v)$ denotes integration of product $uv$ over the volume $\Omega$. To reduce the order of differentiation, the following Green's identity is used (Biro, 1999; Velimsky, 2003):

$$\left(\boldsymbol{\alpha}_j, \nabla\times\upsilon\nabla\times\boldsymbol{\alpha}_i\right)=\left(\upsilon\nabla\times\boldsymbol{\alpha}_i, \nabla\times\boldsymbol{\alpha}_j\right)-\left\langle\upsilon\nabla\times\boldsymbol{\alpha}_i, \boldsymbol{n}\times\boldsymbol{\alpha}_j\right\rangle; \tag{18}$$

where $< u,v >$ denotes a surface integral over $\Gamma$, the boundary of $\Omega$. The unit vector normal to $\Gamma$ is $\boldsymbol{n}$. Equation (18) reduces the second order derivatives of the basis functions to first order derivatives. The surface integral in equation (18) vanishes if

homogeneous Dirichlet boundary conditions are set on $\Gamma$. Recognizing $\boldsymbol{E}_p = -\left(i\omega\boldsymbol{A}_p + \nabla V_p\right)$ and $\boldsymbol{B}_p = \nabla \times \boldsymbol{A}_p$, equation (17) reduces to

$$\sum_{i=1}^{M} a_i \left[\left(\nabla \times \boldsymbol{\alpha}_j, \upsilon \nabla \times \boldsymbol{\alpha}_i\right) + \left(i\omega\sigma\boldsymbol{\alpha}_j, \boldsymbol{\alpha}_i\right)\right] + \sum_{k=1}^{N} b_k \left(\sigma\boldsymbol{\alpha}_j, \nabla\psi_k^c\right) = -\left(\nabla \times \boldsymbol{\alpha}_j, \upsilon_s \boldsymbol{B}_p\right) + \left(\boldsymbol{\alpha}_j, \sigma_s \boldsymbol{E}_p\right). \tag{19}$$

Using the primary fields ($\boldsymbol{E}_p$, $\boldsymbol{B}_p$) instead of the primary potentials ($\boldsymbol{A}_p$, $V_p$) in the right hand side of equation (19) eliminates the need to calculate ungauged primary potentials (G. Wilson, *pers. comm.*). Equation (14) is expressed using $\psi_j$ as nodal test functions in the weak formulation,

$$-\left(\psi_j, \nabla \cdot \left[i\omega\sigma \sum_{i=1}^{M} a_i \boldsymbol{\alpha}_i + \sigma\nabla \sum_{k=1}^{N} b_k \psi_k\right]\right) = -\left(\psi_j, \nabla \cdot \sigma_s \boldsymbol{E}_p\right). \tag{20}$$

Using the identities,

$$\left(\psi_j, \nabla \cdot \sigma\nabla\psi_k\right) = -\left(\sigma\nabla\psi_j, \nabla\psi_k\right) + \left\langle \sigma\psi_j, \boldsymbol{n} \cdot \psi_k \right\rangle$$

and

$$\left(\psi_j, \nabla \cdot i\omega\sigma\boldsymbol{\alpha}_i\right) = -\left(i\omega\sigma\nabla\psi_j, \boldsymbol{\alpha}_i\right) + \left\langle i\omega\sigma\psi_j, \boldsymbol{n} \cdot \boldsymbol{\alpha}_i \right\rangle$$

and setting the surface integrals to zero in the above pairs of equations due to the homogeneous Dirichlet boundary conditions, equation (20) can be expressed as,

$$\sum_{i=1}^{M} a_i \left(i\omega\sigma\nabla\psi_j, \boldsymbol{\alpha}_i\right) + \sum_{k=1}^{N_2} b_k \left(\sigma\nabla\psi_j, \nabla\psi_k\right) = -\left(\sigma_s \nabla\psi_j, \boldsymbol{E}_p\right). \tag{21}$$

Equations (19) and (21) constitute the coupled weak formulation. They reduce to algebraic equations, after the integrations are performed, and can be assembled into a linear system $\boldsymbol{L}u=\boldsymbol{f}$.

### 3.2 Assembling the RHS vector and solving the FE system

The resulting finite element stiffness matrix, $\boldsymbol{L}$, is sparse, and complex symmetric. The integrations on the left hand side of equations (19) and (21) are computed analytically using the reference tetrahedron method outlined in Velimsky (2003). The right hand side is calculated using a 14–point Gaussian quadrature using the coefficients of Jin (2002). I use the QMR solver described by Freund et al. (1992) as implemented by Badea et al. (2001) to solve the system $\boldsymbol{L}u=\boldsymbol{f}$. As mentioned before and shown in Figure 3, the primary fields, $\boldsymbol{E}_p$ and $\boldsymbol{B}_p$, are selected as those due to a homogeneous, conductive, permeable half space excited by an overlying horizontal current loop (Figure 3). Their numerical computation involves the calculation of $J_1$ – and $J_0$ – Hankel transforms. The expressions for $\boldsymbol{E}_p$ and $\boldsymbol{B}_p$ (Ward and Hohmann, 1988) are given below:

$$\boldsymbol{E}_p^{air} = \boldsymbol{\theta}\frac{-i\omega\mu_0 Ia}{2}\int_0^\infty \left[e^{\lambda(z-h)} + \beta e^{-\lambda|z+h|}\right] J_1(\lambda a) J_1(\lambda r) d\lambda \qquad 0 \geq z; \tag{22a}$$

$$\boldsymbol{E}_p^{earth} = \boldsymbol{\theta}\frac{-i\omega\mu_0 Ia}{2}\int_0^\infty \left[1+\beta\right] e^{-(\lambda h + i\gamma z)} J_1(\lambda a) J_1(\lambda r) \lambda d\lambda \qquad z > 0; \tag{22b}$$

$$\boldsymbol{B}_p^{air} = \frac{\mu_0 Ia}{2}\int_0^\infty \left[e^{\lambda(z-h)} + \beta e^{-\lambda|z+h|}\right] J_1(\lambda a)\lambda\{-J_1(\lambda r)\boldsymbol{r} + J_0(\lambda r)\boldsymbol{z}\} d\lambda \quad 0 \geq z; \tag{23a}$$

$$\boldsymbol{B}_p^{earth} = \frac{\mu_0 Ia}{2}\int_0^\infty \left[1+\beta\right] e^{-(\lambda h + i\gamma z)} J_1(\lambda a)\lambda\{-J_1(\lambda r)\boldsymbol{r} + J_0(\lambda r)\boldsymbol{z}\} d\lambda \quad z > 0. \tag{23b}$$

Here, (***r***, ***θ***, ***z***) constitutes the unit vectors of a cylindrical coordinate system whose origin is at the center of the loop; $a$ is the radius of the loop; $\gamma = \sqrt{k^2 - \lambda^2}$ ; $k^2 = -i\omega\mu\sigma$ ; and $\beta$ is the reflection coefficient given by

$$\beta = \frac{\mu\lambda - i\mu_0\gamma}{\mu\lambda + i\mu_0\gamma}. \tag{24}$$

Guptasarma and Singh (1997) developed and described the digital filters which have been used to compute the $J_1$ – and the $J_0$– Hankel transforms.

**3.3 Post processing– calculating fields from potentials**

It must be noted that solving the FE system described in the preceding sub sections (3.1 and 3.2) yields the scalar coefficients $a_i$ and $b_k$ of, respectively, the edge basis vectors defined in equation (9*b*) and the nodal basis functions defined in equation (15*a*). In geophysical surveys using a horizontal loop receiver, the measured response is proportional to $B_z$. The post – processing steps include the calculation of $A_x$, $A_y$, followed by their spatial differentiation which, according to equation (7*a*), yields the sought – after quantity, $B_z$. The post – processing procedure requires a careful analysis of the edge basis functions. The tangential component $A_{tan}$ of a vector potential ***A*** directed along an edge of a tetrahedral element is constant along the edge. A discontinuity in $A_{tan}$ is encountered however at the nodes of the mesh (Dibben and Metaxas, 1997). Nevertheless, it is required to compute the vector potential ***A*** at the nodes to enable a comparison with node – based numerical techniques (Stalnaker, 2004). Thus, unlike the situation in node–based FE, the post processing of edge–based FE is non – trivial and requires additional computational steps. Several schemes have been proposed (Dibben

and Metaxas, 1997; Davidson, 2000; Vollaire et al. 2005). The method outlined below follows Dibben and Metaxas (1997) but while they advocate weighting by the number of edges connected to a given node, in this study better results are obtained weighting by the number of connected tetrahedra.

Thus, using equations (15c), (16*a*), and (16*b*), for a single tetrahedral element, the edge basis vector $\boldsymbol{\alpha}_i$ directed from node *a* to node *b*, and evaluated at node *a*, is expressed as

$$\boldsymbol{\alpha}_i(\boldsymbol{r})\big|_{\boldsymbol{r}=\boldsymbol{r}(a)} = \nabla\psi_b. \tag{25a}$$

The gradient of a nodal basis function is constant inside a given tetrahedron (Slivester and Ferrari, 1996). If the *i* – th edge with nodes (*a*,*b*) belongs to a total of *P*- tetrahedra and node *a* is shared by a total of *M*- edges, then

$$\boldsymbol{A}_s(\boldsymbol{r})\big|_{\boldsymbol{r}=\boldsymbol{r}(a)} = \sum_{i=1}^{M} a_i \sum_{i=1}^{M} \frac{\nabla\psi_b}{P}. \tag{25b}$$

Similarly, for node *b*,

$$\boldsymbol{\alpha}_i(\boldsymbol{r})\big|_{\boldsymbol{r}=\boldsymbol{r}(b)} = -\nabla\psi_a. \tag{25c}$$

$$\boldsymbol{A}_s(\boldsymbol{r})\big|_{\boldsymbol{r}=\boldsymbol{r}(b)} = -\sum_{i=1}^{M} a_i \sum_{i=1}^{M} \frac{\nabla\psi_a}{P}. \tag{25d}$$

Thus, the computation of the vector potential $\boldsymbol{A}$ – at a node can be accomplished by identifying the number of tetrahedra and edges shared by the node. It is also important to determine whether the edge vector $\boldsymbol{\alpha}_i$ is pointing toward node *a* or toward node *b* and accordingly use either equation (25b) or (25d). This approach differs from Dibben and

Metaxas (1997) who advocate normalization by the number of connected edges $M$ instead of the number of connected tetrahedra $P$.

Once the vector potential $\boldsymbol{A}$ is computed at a given node, the field component $B_z$ is readily obtained from equation ($7a$) using a 3 – point central difference scheme (eg. Faires and Burden, 1998).

# 4. VALIDATION OF CODE FORMULATION AND IMPLEMENTATION

The formulation and implementation of a new forward modeling algorithm must be verified against known equivalent solutions. In this dissertation code validation exercises have been divided into two steps : i) a check against non magnetic ($\mu_r = 1$) analytic and numerical solutions and ii) a comparison for the magnetic case ($\mu_r > 1$) against the analytic solution of a magnetic dipole exciting a permeable conducting sphere in free space (eg. Rai and Verma,1982). All edge–based FEM solutions presented here have been tested for convergence on progressively finer meshes and the solutions shown are the ones on the finest mesh that could be supported on our computational platform, a 2.8 GHz 4-core processor with 16 GB RAM.

For the non–magnetic case, I compare results against: a known analytic solution for the 1–D layered earth problem (Ryu et al., 1970; Wait, 1982); a 1–D analytic solution for an equatorial loop current excitation of a homogeneous sphere (Everett and Martinec, 2003); published 2.5–D finite element solutions (Song and Kim, 2009); and finally, fully 3–D node – based finite element solutions (Stalnaker, 2004).

## 4.1 Validation against 1–D layered earth solution

For the layered earth validation, a 4m thick conductive layer (0.1 S/m) located between upper and lower resistive layers (0.02 S/m) is considered. The model strata are excited by a circular loop of 3m radius carrying 1A current at 7 kHz (Figure 5*a*) frequency. The thickness of the upper layer is also 4 m. I use the edge–based FE code to compute the CSEM response for a similar model, namely a 4m thick slab buried at 4m depth and positioned directly beneath the loop (Figure 5*b*). As the slab width increases,

its response should converge to that of the 1–D layered earth. The FE algorithm implements homogeneous Dirichlet boundary conditions, which preclude placing conductive, permeable bodies on the outer computational boundary. To ensure a rigorous test, I subtract from the analytic layered earth solution the background field due to a half space of conductivity 0.02 S/m. This secondary analytic field is then compared against the FE–computed secondary field of the conductive slab. The results are summarized in Figure 6. As the width of the slab increases from 8 m, to 12 m, to 16 m, the FE–computed slab response approaches the analytic layered earth response. The "dip" in the response amplitude (Figure 6*a*) is expected and its location corresponds to the edge of the slab. The trend of the phase response tracks that of the analytic 3- layer solution (Figure 6*b*), keeping in mind the $180^0$ phase change at the edge of the slab. The observed differences between the FE–computed and analytic response curves are due to the finite extent of the slab, which acts much like a secondary vertical magnetic dipole source. The behavior of the FE–computed response in Figure 6 illustrates the limits to which 1D solutions can be used to approximate the response of a three dimensional earth.

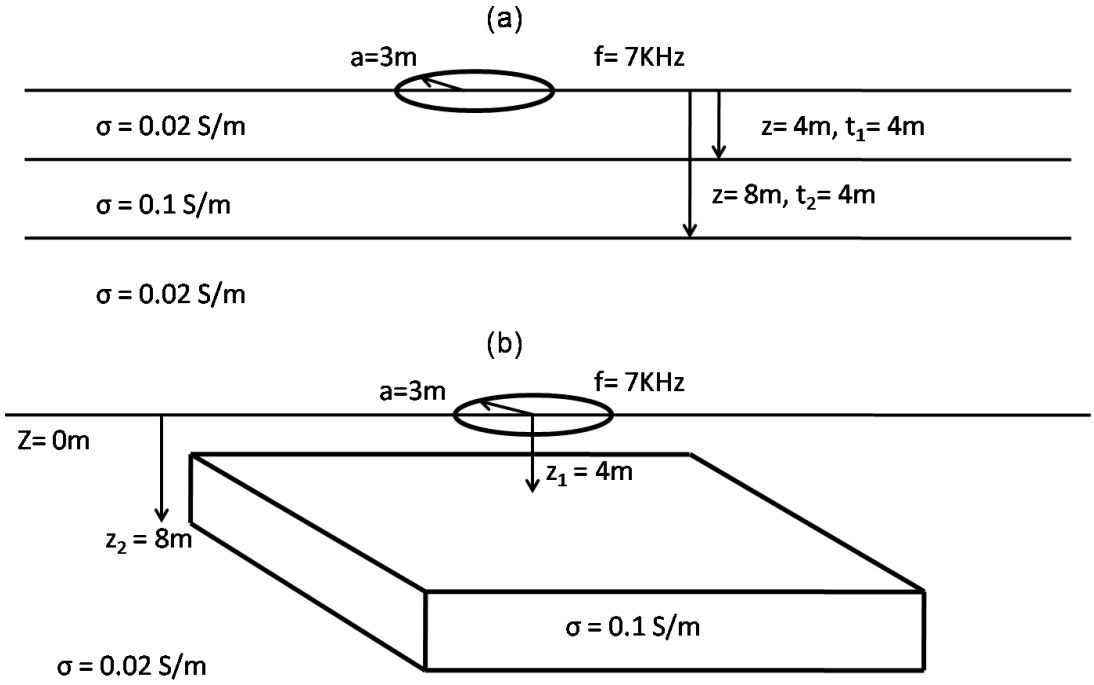


**Figure 5.** (*a*) Schematic representation of the 1-D layered earth problem. (*b*) A slab used to approximate a three layered earth problem.

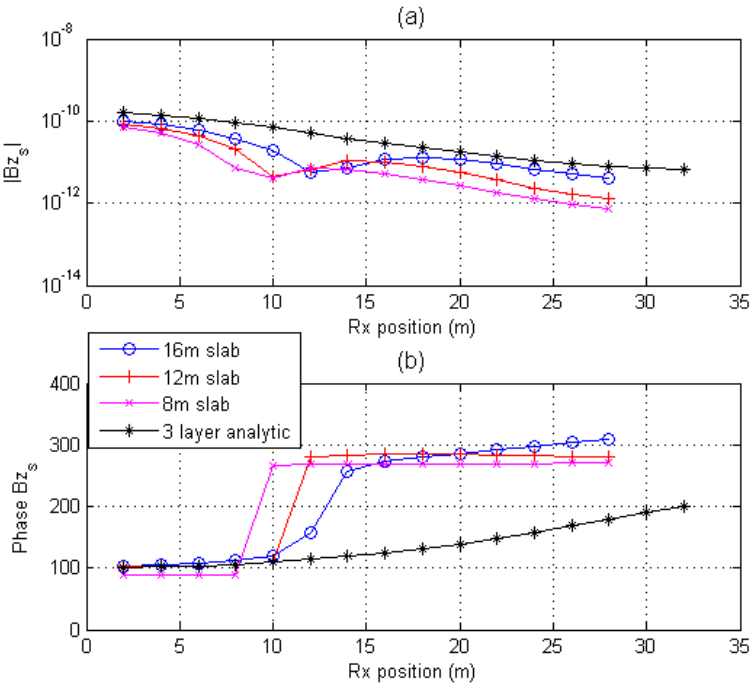


**Figure 6.** Comparison between edge based finite elements and analytic 1–D layered earth solutions at 7 kHz frequency. The transmitter is placed at Rx position 0m. (*a*) The amplitude for different slab widths and the analytic solution for three layer earth. (*b*) The phase for the same problem. The FE–computed and the analytic diverge at Rx positions beyond the slab's lateral termination. At those locations the 1–D approximation is less valid.

### 4.2 Equatorial loop current excitation of a homogeneous sphere

Everett and Martinec (2003) present an analytic solution for induction in a non–magnetic, conducting sphere excited by an equatorial loop current (Figure 7*a*). As mentioned earlier, a rectilinear mesh consisting of tetrahedral elements with an option for local mesh refinement is ideally suited for discretization of conductive, permeable

rectilinear blocks (Stalnaker, 2004). For accurate modeling however, an FE mesh should conform to material discontinuity (Canann et al. 2000; Zorin, 2006), which in this case is a sphere. Conforming the rectilinear mesh to the geometry of the sphere is not performed here. Instead, an equivalent cube is considered. The top of a 0.2m x 0.2m x 0.2m cube is positioned at a depth of 0.1 m directly under a loop of radius 10 m (Figure 7*b*) excited at a frequency of 5 kHz. The equivalent sphere in this case has a volume equal to that of the cube and is excited by an equatorial ring current of the same 10 m radius. The sphere response is computed at a distance z = 0.1 + $b_{eq}$ above the center of the sphere. Here $b_{eq}$ is the radius of the sphere whose volume is equal to that of the cube. Figure 8 shows the quadrature response of $H_z$ inside the loop along a radial profile compared against the equivalent analytic response. The two solutions are in reasonable agreement.

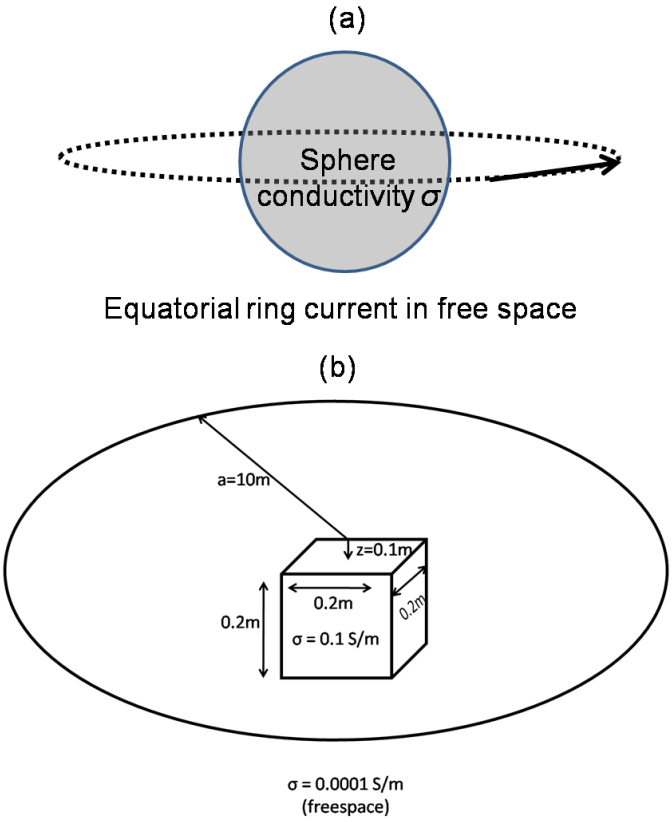


**Figure 7.** (*a*) Schematic representation of the geomagnetic induction problem represented by an equatorial ring current (adapted from Everett and Martinec, 2003); (*b*) schematic representation of electromagnetic induction in a small cube excited by a large axisymmetric loop.

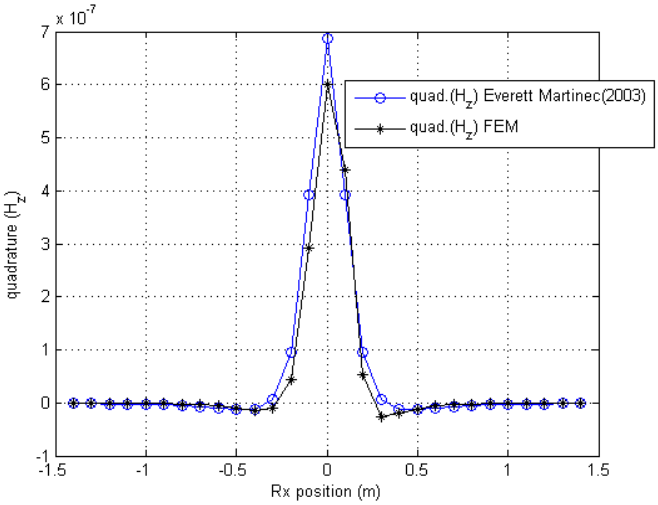


**Figure 8.** Comparison of edge–based FEM against the analytic solution of Everett and Martinec (2003). The conductivity of the cube is 0.1 S/m and is 0.2 m on a side. The loop is placed at Rx position 0 m and height 0.1 m above the top of the cube. The frequency is 5kHz. The quadrature $H_z$ response is presented.

### 4.3 Comparing 2.5–D FEM solutions for a dipole source

Song and Kim (2009) developed a 2.5–D FEM code. They have computed the CSEM response of an infinitely long rectangular pipe with 10 m x 10 m cross section buried 15 m under the surface as shown in Figure 9. The conductivity of the pipe is 0.1 S/m and located within a 0.01 S/m background medium. The sensor is a moving transmitter receiver (Tx–Rx) system with fixed separation $L$ = 40m. Both source and receiver are vertical magnetic dipoles. The system response is plotted at the center of the Tx–Rx configuration. The edge–based 3–D FE code developed in this work models the response of a slab of finite strike length with a 10 m x 10 m cross section due to a finite loop source. Thus the response of a 3–D finite slab excited by a 3–D finite loop shall

approximate the 2.5–D solutions for a vertical magnetic dipole source when the two following conditions are met : (i) the strike length of the finite slab is “long” enough to approximate an infinitely long pipe and (ii) the loop radius and the current flowing through it approximates the dipole strength. To test the effect of (i) different slabs of varying strike lengths have been tested by a 3m radius loop carrying a current of 0.8 A. For (ii), a slab of 80 m strike length is excited by loops of varying radius and current strengths. Song and Kim (2009) computed the normalized impedance defined as

$$Z/Z_0 = \frac{B_z total}{B_z\, freespace}. \tag{26}$$

Figure 10 shows the comparison between the quadrature components of the normalized impedance response for the 3–D finite slab of varying strike lengths, 40 m, 80 m, and 160 m and 2.5– D solution of Song and Kim (2009). The squared norm difference shown in panel (b) of Figure 10 drops to less than 1 % as the strike length is increased beyond 80 m. The comparison of the quadrature components for the 2.5–D and 3–D solutions at 3kHz for the two different excitations, one of 1 m radius and current strength 1 A and the other of 3 m radius and current strength 0.8 A is shown in Figure 11. The squared norm differences shown in Figures 11 (c) and 11(d) are less than 1% in each case suggesting that the strike length of the slab has a stronger influence on the normalized impedance response.

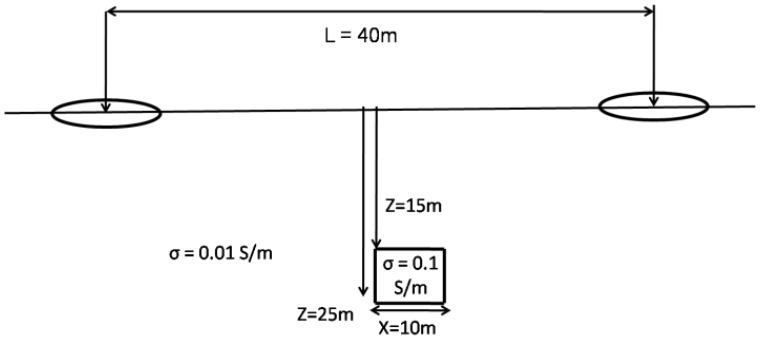


**Figure 9.** A schematic representation of the 2–D block embedded in half space excited by a dipole–dipole system of 40 m separation (Modified from Song and Kim, 2009).

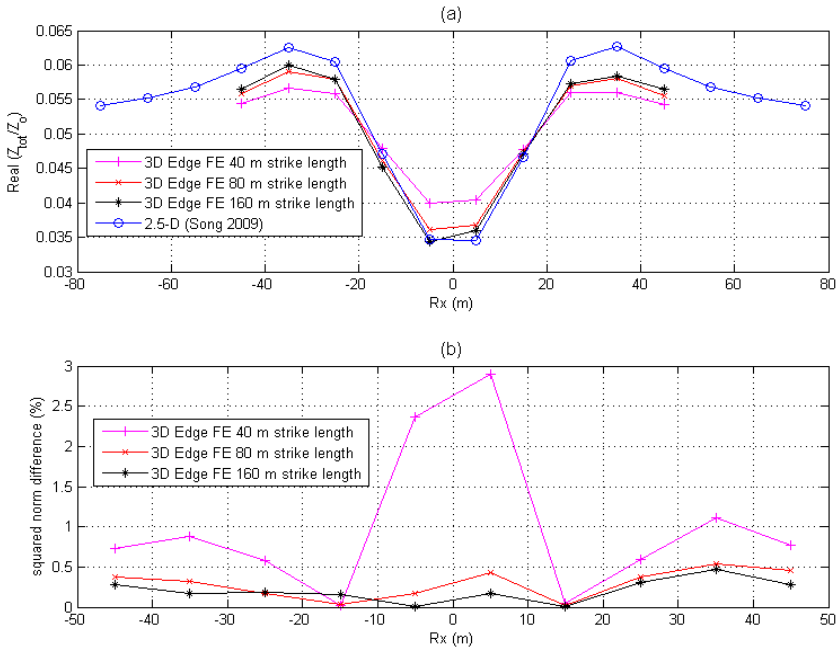


**Figure 10.** (*a*) Comparison between the 2.5–D (dipole source) and 3–D (finite loop source) responses at 3kHz for varying strike lengths of 40, 80, and 160 m. The 3–D finite slab quadrature response approximates that of the 2–D ( infinite strike length) pipe with increasing strike length. (*b*) The corresponding squared norm differences fall to less than 1 % for strike lengths of 80 m and more.

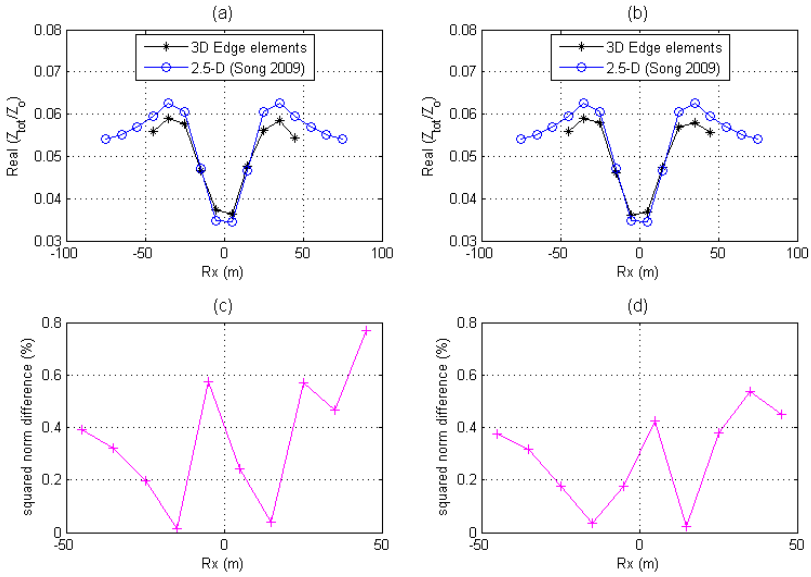


**Figure 11.** Comparison between 2.5–D (dipole source) and 3–D (finite loop source) computed responses at 3kHz for varying loop radius. (*a*) The quadrature components for 1 m loop at current strength 1 A. (*b*) The quadrature components for 3 m loop at current strength 0.8 A. The corresponding misfits are shown in (*c*) and (*d*).

### 4.4 Coulomb gauged node–based FE vs. edge–based FE

Next, I compare two different 3–D FEM implementation formulated with different basis functions and gauge conditions. Stalnaker (2004) developed a 3–D CSEM code using the Coulomb gauge and nodal basis functions. The 3–D CSEM code introduced herein employs ungauged potentials along with mixed edge / node elements. Figure 12 shows the simple model employed for testing. A rectangular slab of dimensions 4 m x 8 m x 4 m buried at 4 m depth with conductivity 0.1 S/m is placed within a homogeneous background of 0.02 S/m. A circular loop of 3m radius and current

1 A is placed on the ground surface ($z$=0). The loop is excited at 0.5, 1.0, and 5.0 kHz. The amplitude and phase of the secondary field component $B_z$ along the x– profile ($y$=0, $z$=0) for these frequencies are displayed in Figure 13. It is well known (eg. Ward and Hohmann, 1988) that the far–field decay of $B_z$ scales as $1/r^3$. Accordingly, the computed amplitudes are compared against a scaled $1/r^3$ function. The two solutions are in good agreement.

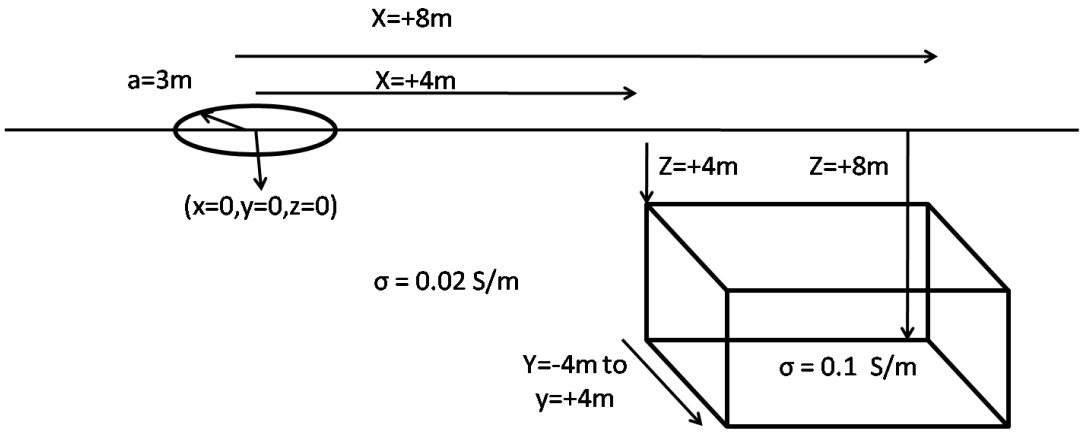


**Figure 12.** A schematic representation of the model used for comparing the ungauged edge–based and the Coulomb–gauged node–based FE implementations.

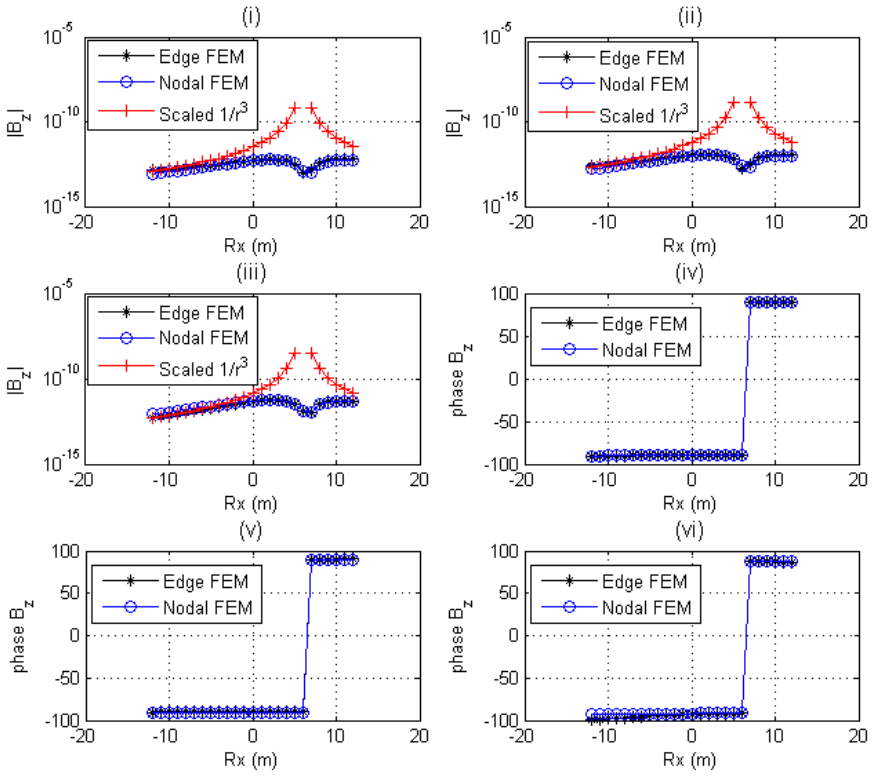


**Figure 13.** Comparison between edge–based, and node–based FE implementations at various frequencies. Panels (*i*)–(*iii*) show the amplitude response for frequencies 0.5, 1, and 5 kHz respectively. The red curve is a scaled $1/r^3$ response. Panels (*iv*)–(*vi*) show the phase response for the same three frequencies.

### 4.5 Analytic solution for a magnetic, permeable sphere in free space

Finally the code is tested for the variable $\mu$ case, which is one of its important new features. The scarcity of published solutions confines the tests to free – space solutions for a conducting, permeable sphere excited by an oscillating dipole (Grant and West, 1965; Lodha and West, 1976; Best and Shamas, 1979; Rai and Verma, 1982). I

choose the solution of Rai and Verma (1982) for its clarity in defining the secondary $H_z$ field. The excitation is a radially directed oscillating dipole (Figure 14*a*). A cube is located directly under a loop source of radius ~3-5 times smaller than the cube length (Figure 14*b*). Figure 15 compares the response of a cube of 8 m side whose top is 4 m under a loop of 1 m radius, oscillating at 50 Hz, against the analytic responses of several concentric spheres whose common center is located 8 m under the loop. Figure 16 presents results with the cube at the same depth against a 4 m radius sphere whose center moves from 5 m to 7 m under the loop. After a few trials I find that a sphere of radius 3.6 m buried at a depth of 6 m produces an equivalent response to that of an 8m cube whose top is at 4m depth from the loop. I have checked this result at various frequencies (0.05 – 5 kHz) and conductivities (0.1 – 10 S/m) and in all cases find reasonable agreement between the FEM and the analytic solutions using the same equivalent sphere.

Having established the robustness of the equivalent sphere over a range of frequency and conductivity, I now compare the sphere and cube responses for the magnetic ($\mu_r > 1$) case. A comparison is made for relative permeabilities $\mu_r$ = 1, 3, 5, 10, and 50 at a frequency of 50 Hz. The results are summarized in Figure 17. There is reasonable agreement between the analytic and the FEM solutions in both amplitude and phase especially at lower permeability.

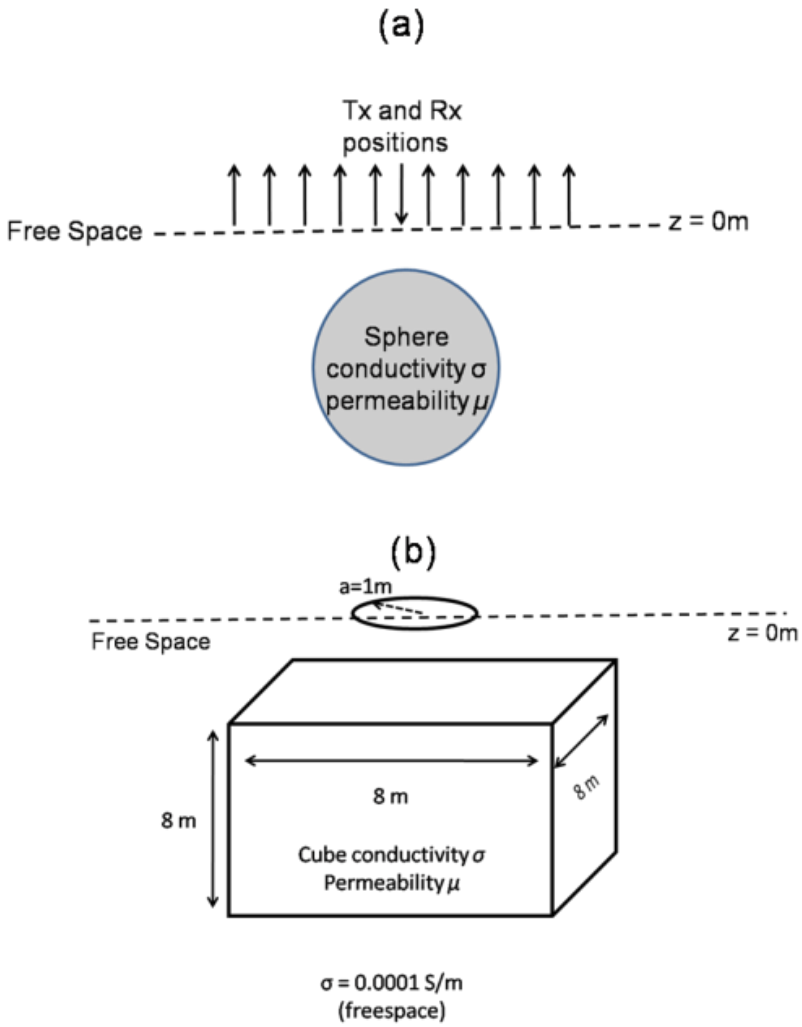


**Figure 14.** (*a*) A conducting, permeable sphere excited by a radial dipole in free space (Rai and Verma, 1982). The *z*- component of the radial and tangential components of the magnetic field is measured at the receiver. (*b*) Schematic diagram of a cube being excited by a small loop source so that the dipole approximation can be used.

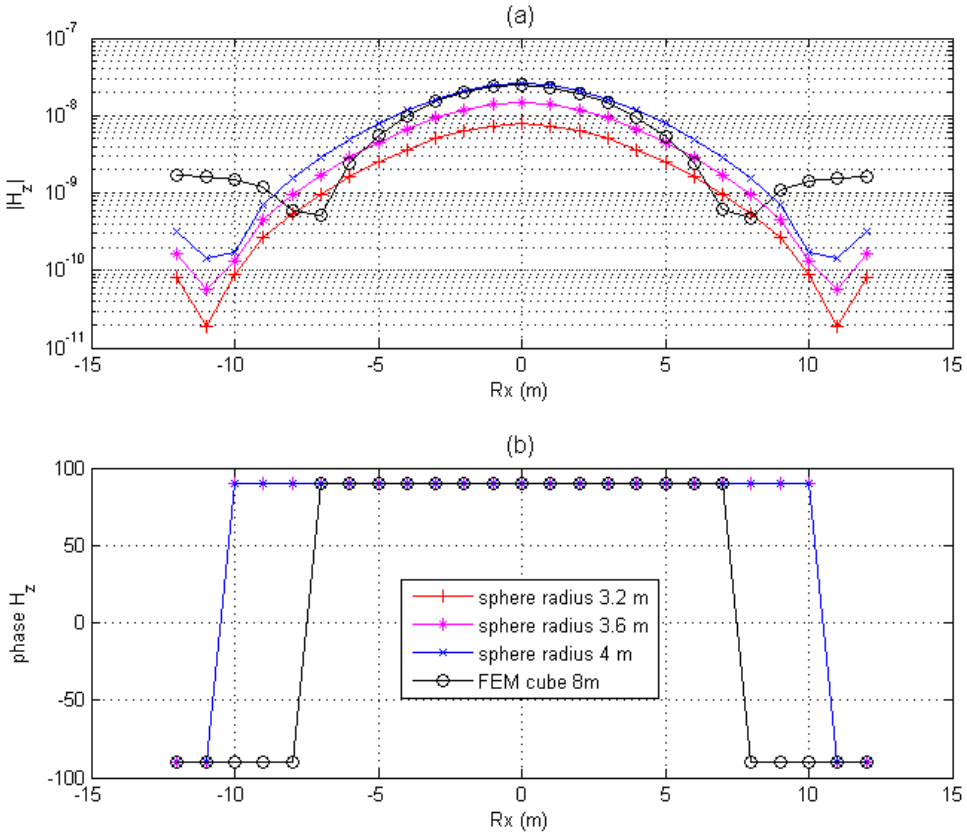


**Figure 15.** A comparison of the responses of concentric spheres whose centers coincide with an 8m cube. The top panel is amplitude, the lower panel is phase.

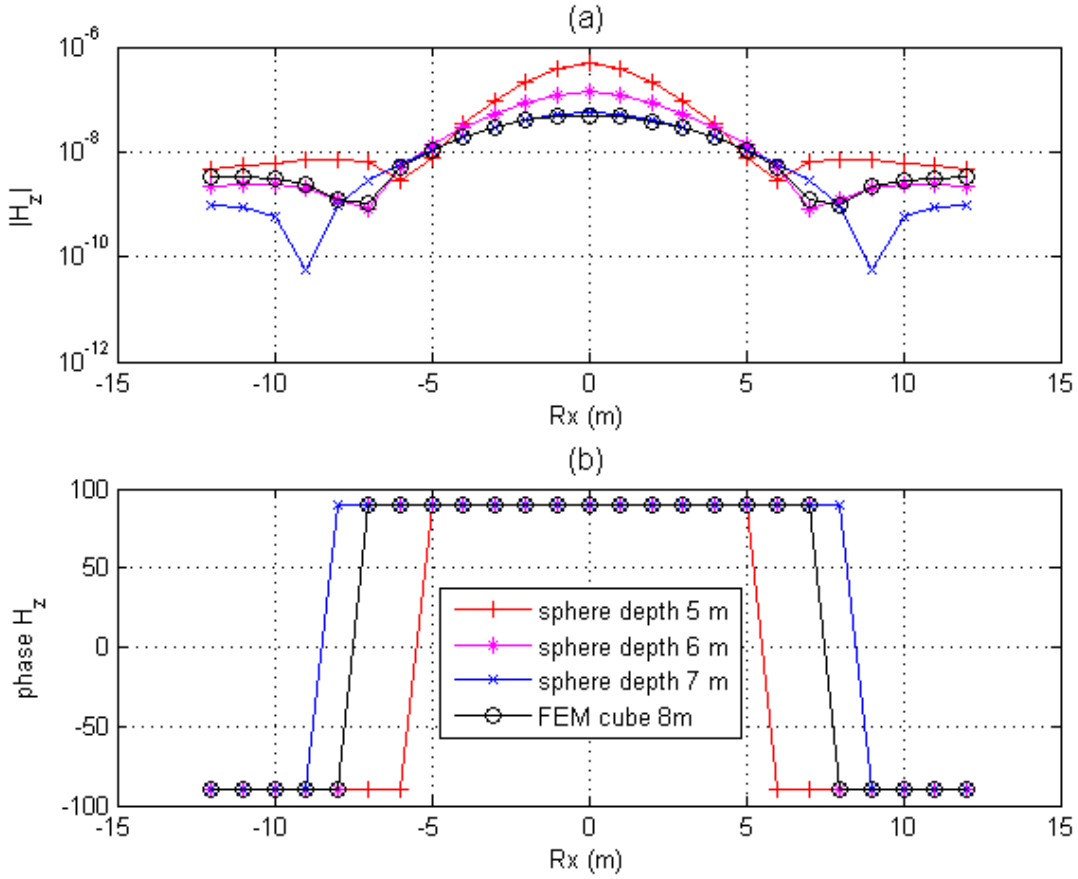


**Figure 16.** Comparison of the response of a 4m radius sphere at varying depths against that of an 8m cube whose top is located 4 m under the loop. The top panel is amplitude, the lower panel is phase.

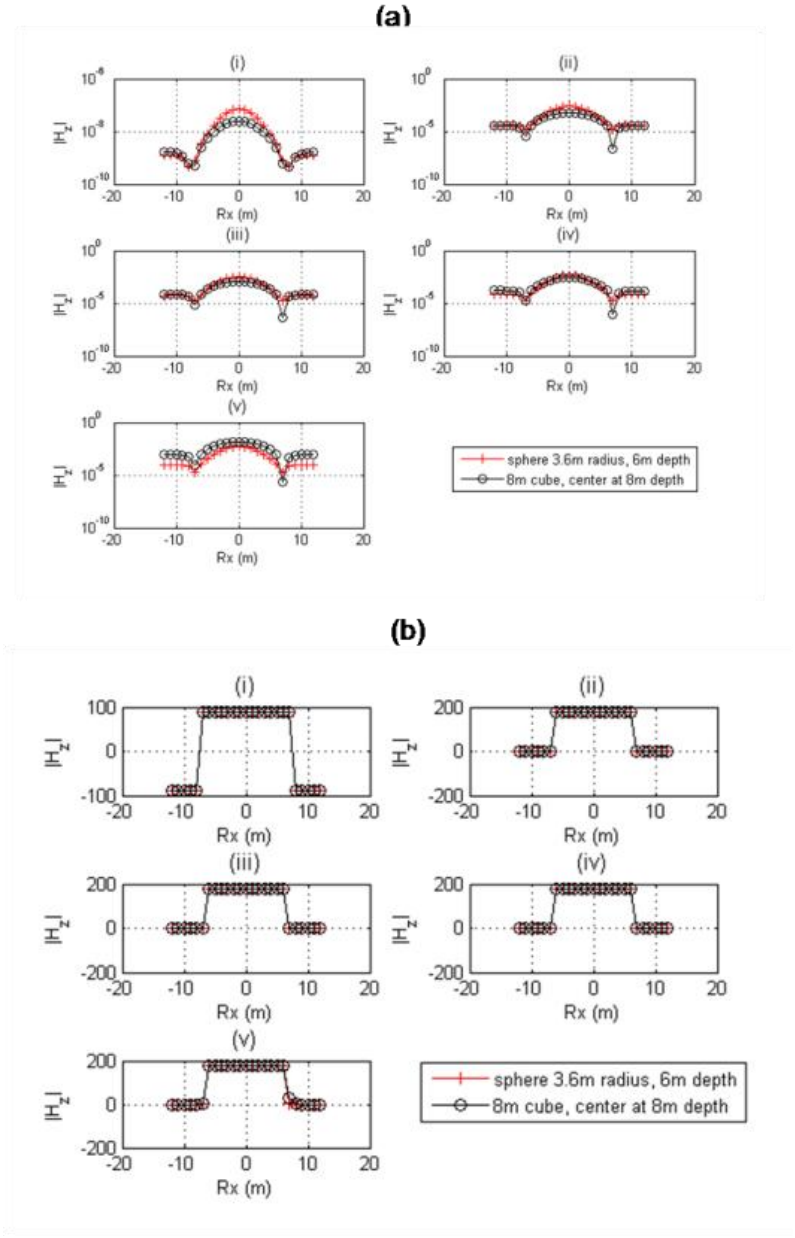


**Figure 17.** Comparison of the response of sphere of 3.6 m radius located at a depth of 6m with that of an equivalent 8 m cube whose top is located 4 m under the loop. Curves are shown for various relative permeability ($\mu_r$) values. (*a*) Panels (*i*) – (*v*) represent the $H_z$ amplitude at frequency 50 Hz, for $\mu_r$ =1, 3, 5, 10, and 50 respectively. (*b*) Panels (*i*) – (*v*) represent the 50 Hz $H_z$ phase response for same set of $\mu_r$.

**4.6 Discussion of results and code performance**

The edge–based FEM technique based on an ungauged potential formulation developed herein has been validated against 1–D analytic and multidimensional numerical solutions. While the new algorithm gives satisfactory solutions over a reasonable range of frequencies, conductivities, and permeabilities, the fits degrade at higher values of these three parameters. A contributing factor is the convergence performance of the QMR solver, which is neither monotonous nor guaranteed for the solution for a cube excited by a small loop, converges slowly at higher values of permeability. Figure 18 shows the QMR convergence as a function of iteration. After 5000 iterations, the convergence for the $\mu_r = 50$ case is several orders of magnitude slower than at $\mu_r \leq 10$. Similar behavior is noted for conductivity and frequency variations. Other situations where the QMR solver is slow or fails to converge to an acceptable level include: (a) Electrically large computation domain (greater than two skin – depths in any one dimension) and (b) highly permeable small targets placed very close to a large loop. The poor convergence is caused by an ill conditioned FE matrix, an unstable right hand side vector, or both. For the former, the use of enhanced preconditioning such as ILU decomposition (Heldring, 2001), or truncated SVD (Berry, 1992) algorithms is recommended. Better approximations to the Hankel transform can improve the stability of the right hand side for large offset and future research may be directed towards either developing improved Hankel transform digital filters or alternative approaches like collocation (Levin, 1996).

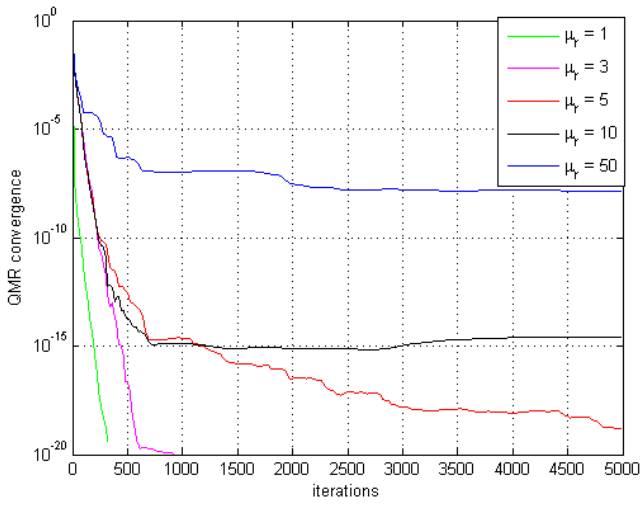


**Figure 18.** Comparing convergence rates for the qmr solver for relative permeability from 1–50 for a 8m side cube of 0.1 S/m conductivity under a small loop (1 m radius) oscillating at 50 Hz in freespace.

### 4.7 Computation speed

As earlier mentioned, the computation platform used in this work is a 2.8 GHz 4-core processor with 16 GB RAM. The finite element algorithm outlined above has several key computational modules. These include: mesh generation, matrix assembly, RHS assembly, matrix solver (QMR), and post processing. Most examples used here for code validation have been discretized using 33 x 33 x 33 nodes in the *x*-, *y*-, and *z*-directions of a uniform mesh with no local mesh refinement. The mesh has 196608 tetrahedra, 35937 nodes, and 238688 edges. The total number of degrees of freedom in the FE system is 250047. Total run time is approximately 8 hours. Table 1 shows the

percentage time approximately used up by the CPU for executing the different modules of the code.

**Table 1.** Relative computational efficiency of the different modules of FE computation.

| **Computational task** | **Percentage time (%)** |
|---|---|
| Mesh generation | 1 |
| Matrix assembly | 7 |
| RHS assembly | 80 |
| Matrix solver (QMR) | 10 |
| Post processing | 2 |

At present a 14 – point Gaussian quadrature is invoked for every tetrahedral element in the mesh for assembly of the RHS vector. The process is far from optimized and as apparent from the above table, improvements in RHS assembly will improve the efficiency of the code dramatically.

# 5. EFFECTS OF MAGNETIC PERMEABILITY ON MUTUAL COUPLING

## 5.1 Introduction

It has been mentioned in Section 1 that the CSEM response of a conducting, permeable geophysical target can be regarded as the summation of inductive and galvanic modes of current excitation, plus a magnetization mode. When two or more such targets are present, then their mutual interactions produce tertiary and higher order current excitation and magnetization modes. Quantifying the induced tertiary currents is useful for understanding the mutual coupling effects between a subsurface target of interest and a "known" cultural element such as a powerline or a metallic fence or two cultural elements. The distortion of the response from a geophysical target due to the presence of cultural elements has long been considered a major obstacle to correct interpretation of CSEM response (e.g. Szarka, 1988; Junge, 1996). Oftentimes geophysicists simply disregard CSEM data that have been distorted by cultural noise.

The mutual impedance (*MI*) formulation of the CSEM response can provide useful insights into the physics of interaction between two subsurface targets or between a single target and host geology (Wait, 1982). It is well known (eg. Wait, 1955) that the mutual coupling between two loops over a heterogeneous earth is dependent on the conductivity distribution of the subsurface. The mutual coupling is expressed as $Z/Z_o$ where $Z$ is the *MI* measured between the coils and $Z_o$ is the same measured in free space. Equation (26) in Section 4 shows that *MI* is the total magnetic field measured in the presence of the Earth normalized by that which would have been measured in free space (Song and Kim, 2009).

$$Z/Z_0 = \frac{B_z total}{B_z\, freespace}. \tag{27}$$

Also, in Section 4 it was shown that a conductive target excited by a primary loop source behaves as a secondary source of current. If two or more conductive targets are present, one of the targets acting as a secondary source induces tertiary electric currents in the other. The concept of mutual coupling between loops has been generalized to study the interaction between two buried conductive targets by Fernandes, (2008) . Stalnaker et al. (2006) earlier demonstrated that the CSEM response of multiple buried targets, or a single target of complex geometry composed of different materials can be significantly influenced by their mutual coupling and interaction with the host geology. In this work, I use the newly developed edge – based CSEM code described in the previous sections to study the influence of magnetic permeability on the mutual coupling of conductive targets of simple shape. This is done to enable a better understanding of CSEM responses acquired at environmental, UXO, or archaeological sites in which multiple buried permeable targets are often found.

**5.2 Overview of mutual coupling between two buried targets**

Qian and Boerner (1994) treat cultural elementsuch as metallic fences, and powerlines as discretely grounded conductors (DGC) and use the theory of grounded circuits to describe the mutual interaction between such structures and the host geology. They quantify the total electric field $\boldsymbol{E}$- inside a conductor as

$$\boldsymbol{E}(\boldsymbol{r_0}) = \boldsymbol{E}^n(\boldsymbol{r_0}) + \int_v \boldsymbol{G}(\boldsymbol{r} \mid \boldsymbol{r_0}) \mid \boldsymbol{j}(\boldsymbol{r}) d\boldsymbol{r}; \tag{28}$$

where $\boldsymbol{E}^n$ is the field that would exist in the absence of the DGC while $\boldsymbol{G}(\boldsymbol{r}|\boldsymbol{r_0})$ is the 3x3 dyadic Green's function for computing the electric field at $\boldsymbol{r}$ due to an electric dipole at $\boldsymbol{r_0}$ and $\boldsymbol{j}(\boldsymbol{r})$ is the current density distribution in the DGC. This integral equation formulation allows the decomposition of an observed CSEM signal into a "geologic" component and a "known" cultural component modeled as a DGC, thereby isolating its influence on the signal.

There are other conceptual approaches to describing mutual coupling between conductive targets such as complex natural resonance (CNR) by Geng et al.(1999) . A standard approach is to consider the magnetic flux linkage between two conductive bodies (eg. Ulaby, 2004). For simplicity, the two bodies can be assumed to behave as two closed loops 1 and 2 as shown in Figure 19. Then, the flux through $L_2$ due to current in $L_1$ is given by

$$\phi_{21} = \int_{S_2} \boldsymbol{B} \cdot d\boldsymbol{s}; \tag{29}$$

where $\boldsymbol{B}$ is the magnetic field generated by the current in loop $L_1$. The mutual inductance $M_{21}$ of loop $L_2$ due to current flowing in $L_1$ is given by (Ulaby, 2004)

$$M_{21} = \frac{\phi_{21}}{I}. \tag{30}$$

The total energy stored in the two loop system is the same irrespective of whether current in $L_1$ induces a field in $L_2$ or vice versa (eg. Alexander and Sadiku, 2004). It can be shown from a consideration of conservation of total energy that

$$M_{21} = M_{12} = MI \tag{31}$$

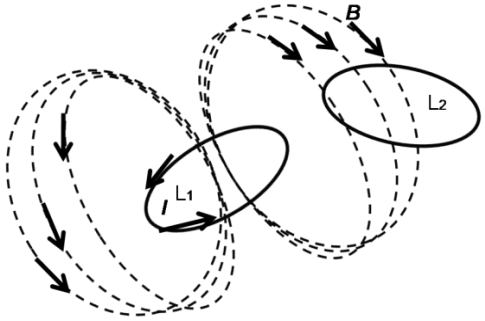


**Figure 19.** Magnetic field ***B*** fluxing through loop $L_2$ due to current ***I*** in loop $L_1$ (Modified from Fernandes, 2008).

In a geophysical field investigation, the magnetic field is measured by a receiver loop of constant area. The magnetic flux threading the loop according to equation (29) is essentially a function of the measured field $B_z$ – while the current according to Ampere's circuital law is proportional to $H_z$. Thus, in equation (30), the effect of mutual coupling (*MC*) between two buried geological targets excited by a unit current can be isolated using the expression (Fernandes, 2008):

$$MC = \left|\mathrm{Im}\left(H_z^1 + H_z^2 - H_z^{(1+2)}\right)\right|; \tag{32a}$$

where *MC* = mutual coupling; $H_z^{(1+2)}$ = secondary $H_z$ response of a model consisting of two targets embedded in a conductive, permeable geologic medium; $H_z^1$ = secondary $H_z$ of the same model containing target 1 without target 2; $H_z^2$ = secondary $H_z$ of the same model containing target 2 without target 1. I also define the term normalized mutual coupling *MCn* in equation (32*b*) as

$$MCn = \left|\mathrm{Im}\left(H_z^1 + H_z^2 - H_z^{1+2}\right)\right| / \max\left|H_z^{1+2}\right| \tag{32b}$$

Fernandes (2008) has numerically modeled the effects of mutual coupling for a range of target conductivities, relative orientations and frequencies. Here, I extend the analysis to include the effects of mutual coupling of *permeable* targets for models of simple shape, namely two cubes buried in a conductive half space.

### 5.3 Numerical estimation of mutual coupling between two buried cubes

The following geometry was used to explore the mutual coupling of conductive, permeable targets excited by a controlled electromagnetic source as modeled by the edge–based finite element algorithm. Two 2 m x 2 m x 2 m cubes are buried 2 m deep in a 0.02 S/m conductive halfspace, as shown in Figure 20. The cubes each have 0.1 S/m conductivity. Their centers are placed 10 m apart and they are excited by a 3 m radius loop of current strength 1A and frequency 50 Hz. The center of the loop is placed on the ground surface ($z$ = 0 m) at the mid–point between the cubes.

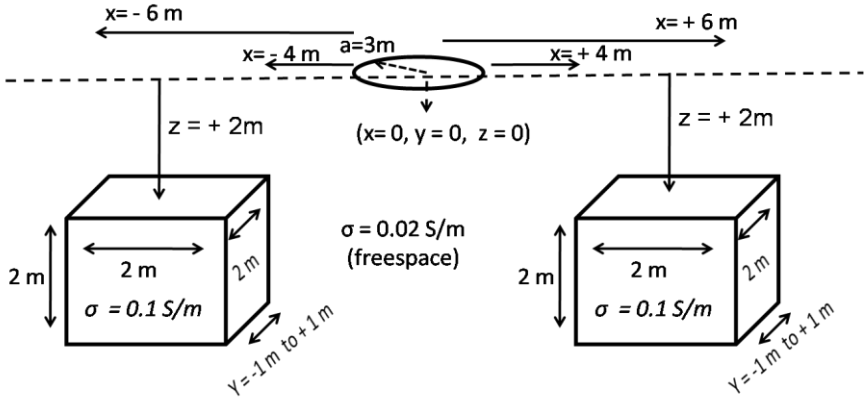


**Figure 20.** Schematic representation of two buried cubes of conductivity 0.1 S/m excited by a 3m loop at 50 Hz. The effect of permeability on their mutual coupling is evaluated by varying the permeability of either one or both cubes.

Table 2 summarizes the electrical and magnetic properties of two different suites of models. In the first suite, the relative permeability of cube A (on the left) is kept constant at $\mu_r = 1$, while that of B is varied from $\mu_r = 1$ through $\mu_r = 20$. In the second suite of models, the permeabilities of both cubes are changed simultaneously so that each cube has the same permeability for every forward modeling run. To estimate the *MC* and *MCn* parameters described in equations (32*a*) and (32*b*), three forward modeling runs are necessary to evaluate each row of Table 2; one run for the full two–cube model, one run with only the left cube is present, and one more run for a model containing the right cube only. As described in Section 1, the CSEM response of a nonmagnetic ($\mu_r = 1$) conductive body located in a conductive host can be decomposed into two modes of current excitation which contribute to the secondary magnetic field: the inductive mode, in which the current is confined to circulate inside the conductor, and the galvanic, or current channeling mode in which current gathered from the host medium flows through the conductor. In magnetic ($\mu_r > 1$) bodies, a magnetization mode also contributes to the secondary field. At 50 Hz the right cube is galvanically saturated ($C$=1.25) but inductively undersaturated ($K$=9.87x10$^{-6}$). As the permeability of the right cube is increased, the relative effects of the three modes on the overall field can be assessed using the *MC* and *MCn* formulations described in equations (32*a*) and (32 *b*).

**Table 2.** Model suites for mutual coupling experiments at 50 Hz frequency.

| | Left Cube $\mu_r$ | Right Cube $\mu_r$ |
|---|---|---|
| Model Suite A | 1 | 1 |
| | 1 | 5 |
| | 1 | 7 |
| | 1 | 10 |
| | 1 | 12 |
| | 1 | 15 |
| | 1 | 20 |
| Model Suite B | 1 | 1 |
| | 5 | 5 |
| | 7 | 7 |
| | 10 | 10 |
| | 12 | 12 |
| | 15 | 15 |
| | 20 | 20 |

The forward modeling results, expressed in terms of *MC* and *MCn* for suite A are summarized in Figures 21 through 23. The responses shown in Figure 21 are checked for possible modeling artifacts by interchanging the permeabilities of the left and right cube. The *MC* reciprocal responses should be equal if there are no gross modeling errors. As

shown in Figure 21, the squared norm difference in the *MC* reciprocal responses is less than 1 % for a range of relative permeabilities up to $\mu_r$ = 20.

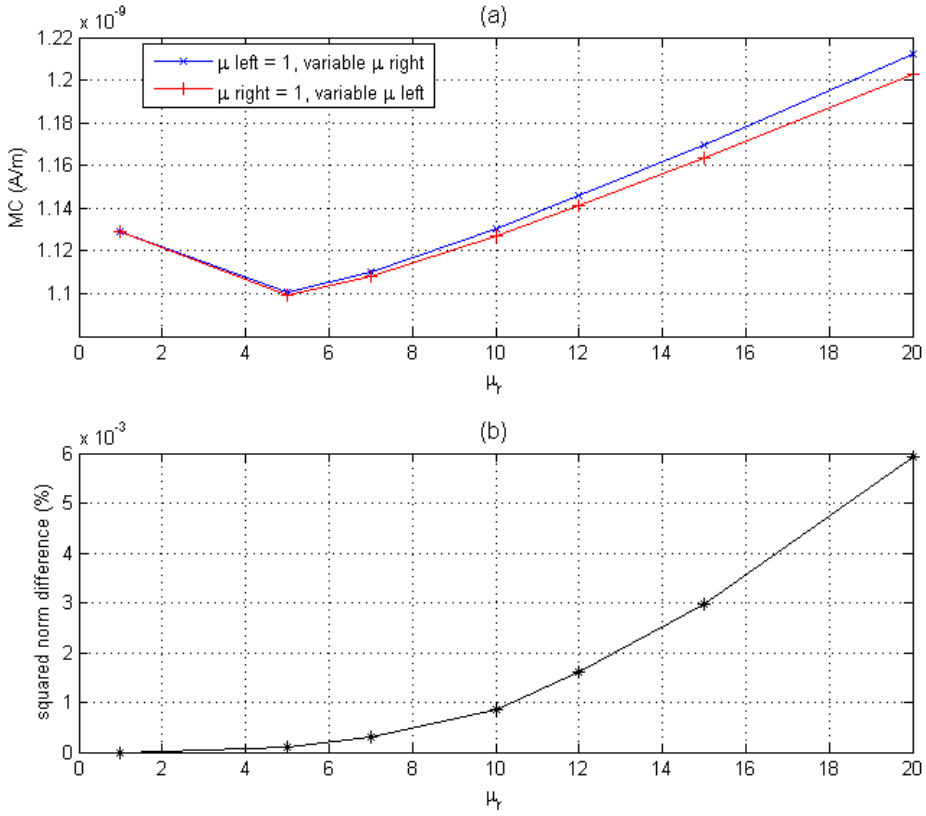


**Figure 21.** Comparing reciprocal *MC* responses for model suite A: (*a*) the blue curve shows the response for the configuration mentioned in Table 2, while the red curve shows the response when the cube permeabilities $\mu_r$ are interchanged. Operating frequency is 50 Hz; (*b*) the relative misfit between the reciprocal cases.

Figure 22 shows the behavior of the mutual coupling coefficient (*MC*) as described by equation (32*a*). The curves are closely spaced above the right cube while

they separate out over the left cube as the right cube becomes more permeable. This result appears to be counter – intuitive but it is actually expected. The contribution to the total field for the permeable right cube comes from a combination of galvanic, inductive, and magnetization modes, whereas the contributions from the non permeable left cube are confined to only the galvanic and inductive modes. Since the host conductivity and the cube conductivity is the same for both cubes, the magnetization mode from the right cube has a dominant residual effect on the subtracted field over the left cube in the *MC* response (equation 32*a*).

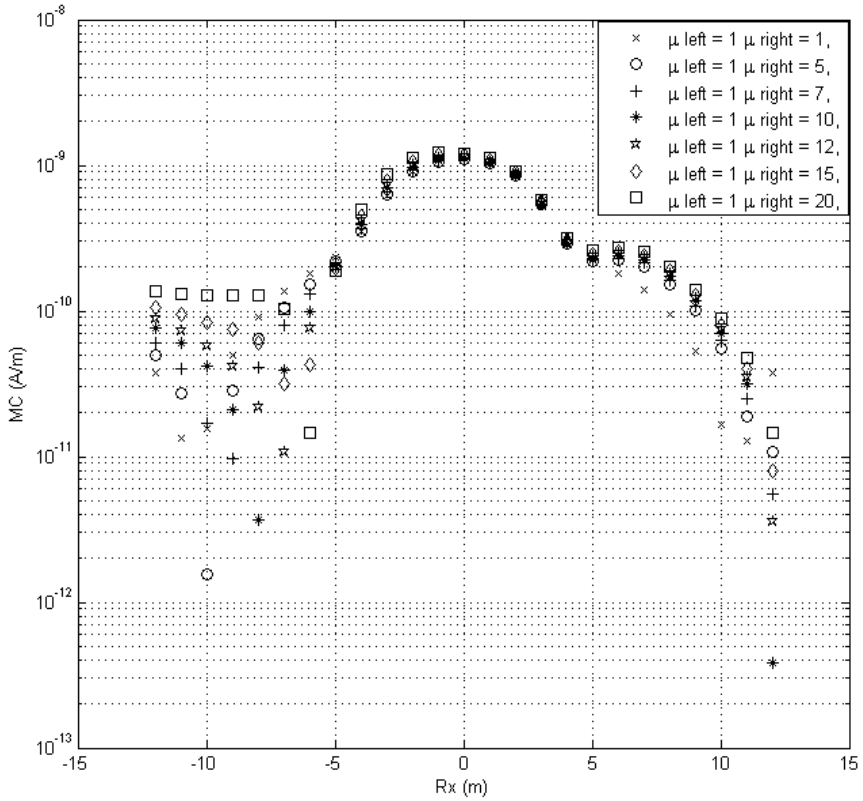


**Figure 22.** *MC* between a non–magnetic and a magnetic cube with increasing magnetic permeability. Operating frequency is 50 Hz.

In practical field experiments it is not feasible to estimate absolute mutual coupling between geologic and man – made structures (Qian and Boerner, 1994) as this would involve measuring the exact response of the geology in absence of the structure. For bulky storage tanks, buried powerline infrastructure, etc., excavation of the cultural target is an impractical exercise. It is thus more useful to calculate the extent of coupling as a percentage of the secondary field according to equation (32*b*). Accordingly, the *MCn* components for model suite A are shown in Figure 23. Interestingly, the magnitude of coupling decreases in proportion to the total measured secondary field with increasing $\mu_r$ for the right cube. Similar effects are observed for model suite B where both left and right cubes have the same $\mu_r$ (Figures 24 and 25). This suggests that higher $\mu_r$ increases the contribution from the magnetization mode discussed in section 1 to the overall field. As discussed in Section 1, the decay time for fields in the magnetization mode is longer and the decaying rate is different from that of the induced eddy current mode (Pasion, 2007). Thus, not only is mutual coupling lower as a proportion of the total field, but also the shape of the curves in Figures 23 and 25 are different from that of the non magnetic case.

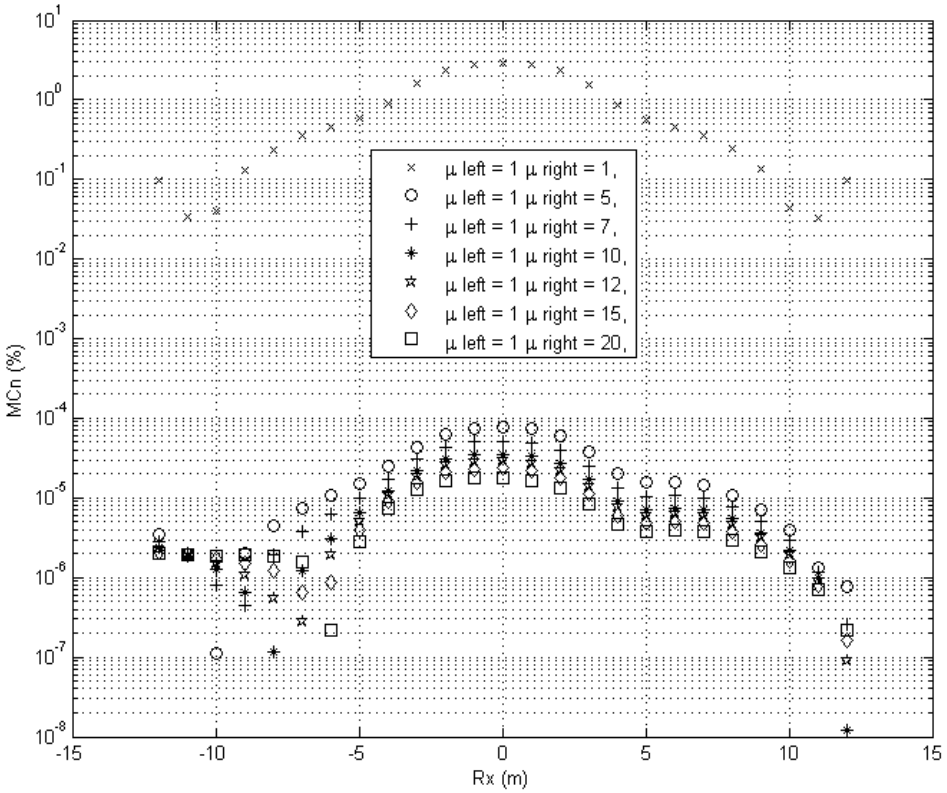


**Figure 23.** *MCn* between a non–magnetic and a magnetic cube with increasing magnetic permeability. Operating frequency is 50 Hz.

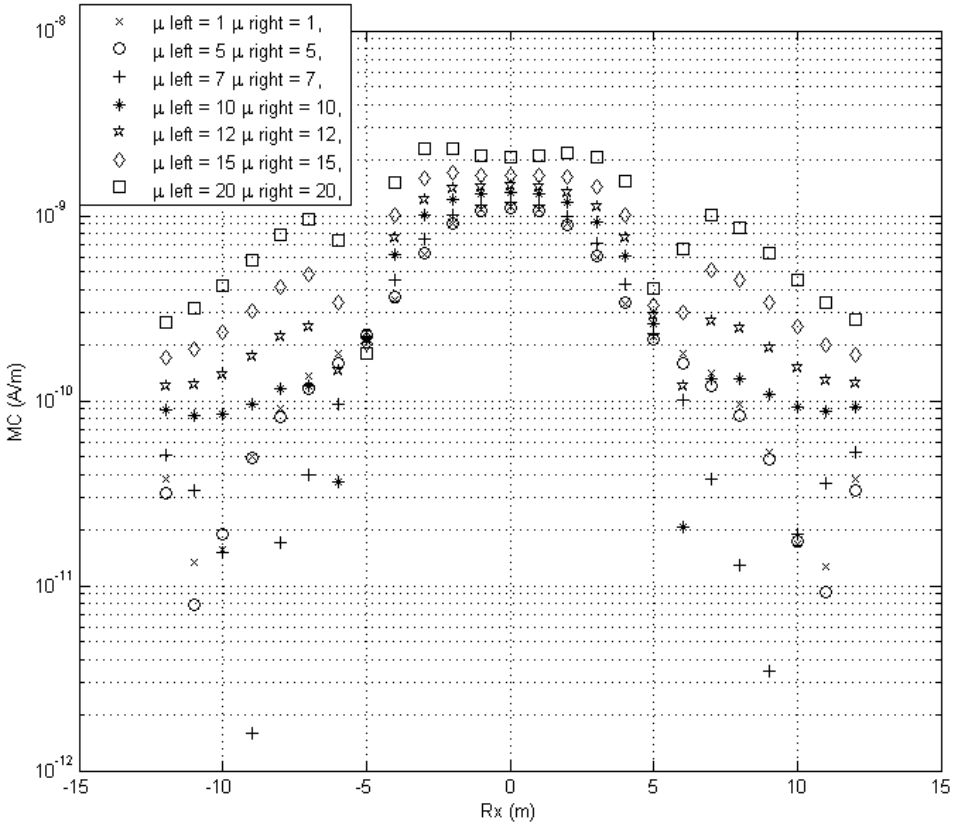


**Figure 24.** *MC* between two magnetic cubes having equal magnetic permeability (model suite B in Table 2). Operating frequency is 50 Hz.

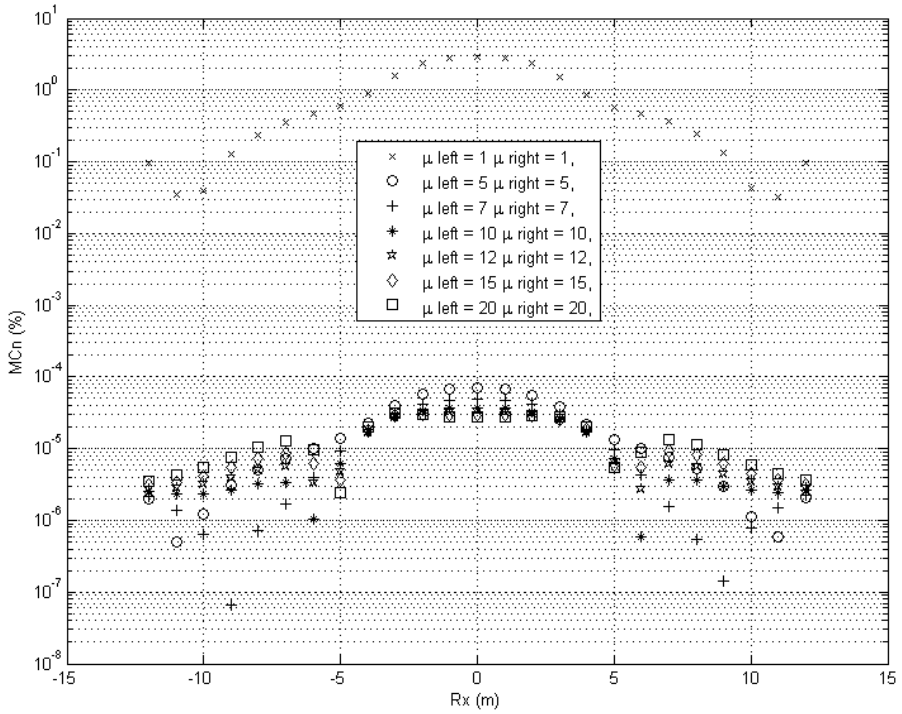


**Figure 25.** *MCn* between two magnetic cubes having equal magnetic permeability (model suite B in Table 2). Operating frequency is 50 Hz.

Next, I investigate the dependence of the mutual coupling of magnetic cubes on the operating frequency. Most cultural refuse present environmental field investigations such as buried metal pipes, steel drums, etc. have an *effective* $\mu_r$ in the range of 1.0 – 1.5 (Barrows and Rocchio, 1990). The effective $\mu_r$ (Grant and West, 1965) is a measure of the net reduced field of a magnetic body due to the effects of demagnetization dependent on the shape of the magnetic body and it's orientation relative to the inducing field. The effective permeability is also reduced for hollow magnetic bodies relative to solid magnetic bodies of the same overall size and shape. The investigation frequencies range

from 100Hz –1MHz (Everett and Meju, 2005). As has been noted in the previous section, the convergence of the QMR solver is slower at higher frequencies and magnetic permeabilities. The code calibration results presented in the previous section generally point towards a minimum acceptable QMR residual of $10^{-8}$. Table 3 summarizes Model Suite C results. This suite of models is run for a number of frequencies to determine the range of model parameters that can be accurately modeled by the edge – based CSEM code. The convergence plots are shown in Figure 26. As evident, models with $\mu_r \leq 1.5$ can be modeled at frequencies of upto 5 kHz for the model geometry specified in Figure 20.

**Table 3.** Model suite C for mutual coupling dependence at higher frequencies.

| | Left Cube $\mu_r$ | | Right Cube $\mu_r$ | |
|---|---|---|---|---|
| Model Suite C | 1 | | 1.0 | |
| | 1 | | 1.3 | |
| | 1 | | 1.5 | |
| | 1 | | 1.7 | |
| | 1 | | 2.0 | |
| | Frequency (kHz) | | | |
| | 1 | 3 | 5 | 7 |

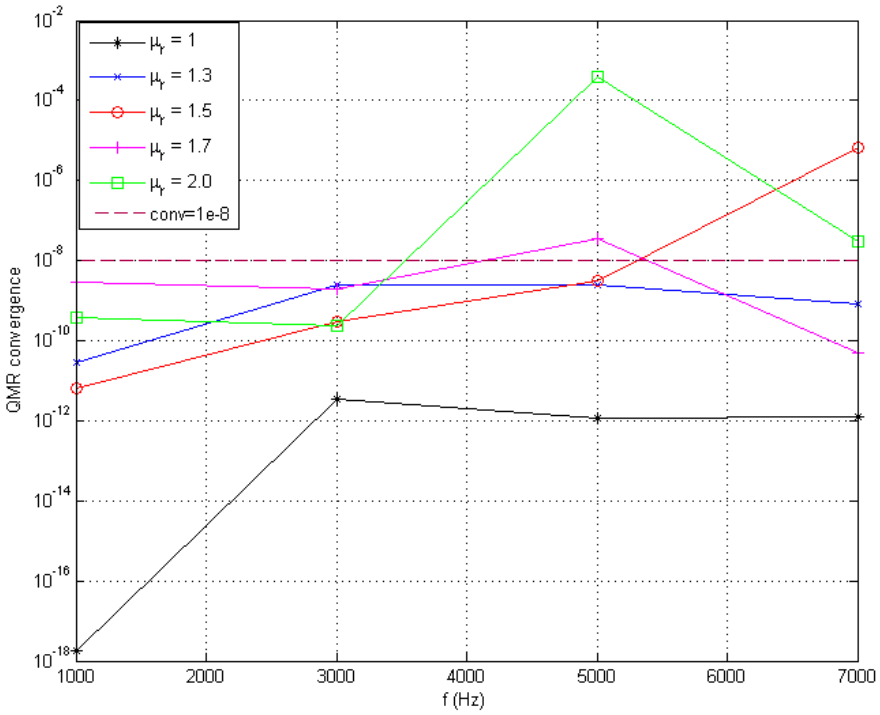


**Figure 26.** QMR convergence for model suite C at various frequencies upto 7 kHz. Acceptable levels of convergence may be achieved upto $\mu_r$ = 1.5 at 5 kHz frequency.

The first three models from suite C of Table 3 have been used for testing the frequency dependence of mutual coupling effects for magnetic bodies. The results are summarized in Figure 27. As evident from Figures 22 – 25, the mutual coupling values are maximum at the center of the loop. Thus, the *MCn* values for model suite C have been plotted at the center of the loop for $\mu_r$ = 1.0, 1.3, and 1.5 for the right cube. There is a peak around 3kHz (~ 9%) for $\mu_r$ = 1.0 while $\mu_r$ = 1.3 has a peak at 2kHz(~ 4%) and a smaller one at 4 kHz (~ 1%). The peaks for $\mu_r$ = 1.5 appear at 2 kHz (~ 1.2%) and another at 5 kHz (~ 0.7%) . The contributions from the magnetization mode for $\mu_r$ > 1

diminishes the effect of inductive mutual coupling on the observed field in the frequency range studied here for this model geometry.

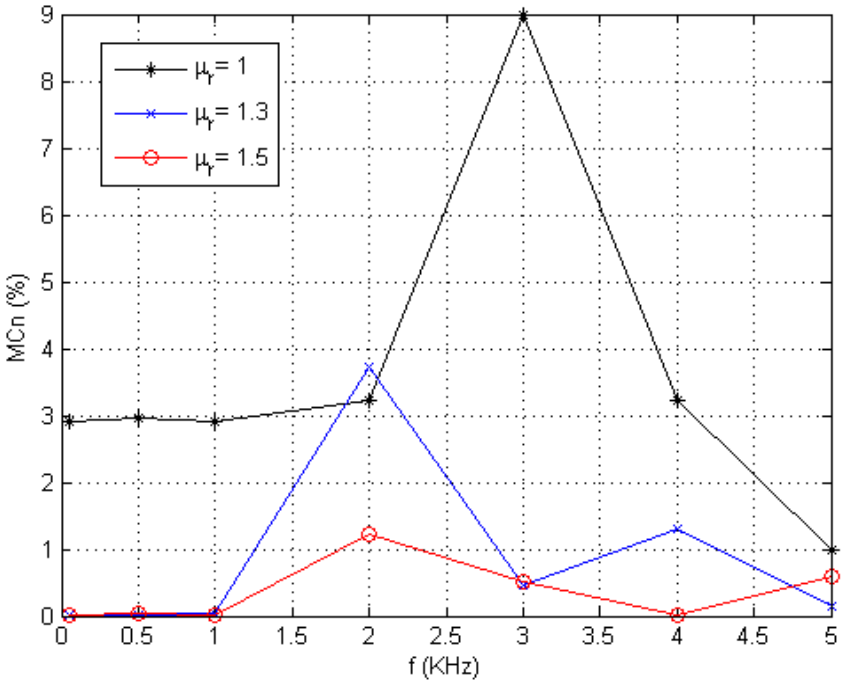


**Figure 27.** *MCn* plots for $\mu_r$ = 1.0, 1.3, and 1.5 plotted at center of the loop (x=0m, y=0m).

### 5.4 Discussion of results

The new edge – based CSEM code can be used to estimate the effects of mutual coupling between cultural targets and host geology. For the simple two–cube models studied here, magnetic permeability diminishes the relative contribution of inductive coupling to the measured field. The main reason for this appears to be an increased contribution from the magnetization mode as discussed in Section 1. The secondary

magnetic field generated by the coupled host – target interaction acts as a source of tertiary eddy currents induced in the target (Fernandes, 2008). The behavior of such fields can be demonstrated in terms of the secondary magnetic field of a conducting permeable sphere excited by an oscillating radial magnetic dipole (a very small loop carrying a harmonic current) in free space (Rai and Verma, 1982) . As seen in Figure 2, the peak of the quadrature response shifts towards lower frequencies with increasing $\mu_r$.

The mutual coupling response as formulated by equations 32*a* and 32*b*, is expressed in terms of the quadrature component of the field response. Thus, for the tertiary currents introduced in the system, there is a corresponding peak in coupling response in Figure 27. For $\mu_r$ = 1, the peak occurs around 3 kHz, while for $\mu_r$ = 1.3 and 1.5, the dominant peaks appear in the vicinity of 2 kHz. The sparsity of data points , due to lengthy computational runs, may have aliased the exact location of the peaks. The smaller peaks associated with $\mu_r > 1$ could be modeling artifacts. Expanding the investigation over a wider range of frequencies with a more robust solver or enhancing QMR performance with an improved pre conditioner may help resolve the issue of the smaller peaks.

# 6. CONCLUSIONS

In this dissertation, I have developed a three–dimensional edge–based CSEM finite element algorithm based on an ungauged, secondary–potential formulation. The algorithm is capable of modeling the CSEM response conductive and permeable structures embedded in piecewise constant idealizations of geologic media. The code has been verified against several analytic and multi–dimensional numerical solutions and generates reliable CSEM responses over a reasonably wide range of frequencies, conductivities, and magnetic permeabilities. The traditional approach of modeling the electromagnetic response of magnetic targets employs a formulation of the governing equations in terms of magnetic susceptibility (eg. Farquharson et al. 2003). Here, a new parameter in geophysics, reluctivity (Biro, 1999), facilitates a separation of primary and secondary potentials.

The code is designed to model near – surface CSEM responses over buried magnetic ($\mu_r > 1$) targets representative of cultural elements such as buried storage tanks, drums, or pipelines. The CSEM response consists of a superposition of inductive, galvanic, and magnetization modes. As "proof of concept", mutual coupling effects between two magnetic bodies and a magnetic and non magnetic body have been studied. The presence of magnetic bodies diminishes the contribution of the inductive coupling between targets to the overall response relative to the contribution from the magnetization mode. This is important for applications in which significant cultural debris may be present. The presence of such buried cultural elements has often been considered a major impediment to accurate geological interpretation of CSEM data.

Some limitations of the code, such as convergence of QMR solutions, meshing of spheroidal and other structures with curvilinear material discontinuities, and computation speed have been noted. Addressing these issues would increase the applicability of the code to higher frequencies, conductivities and permeabilities, which are relevant for certain environmental geophysics problems such as UXO discrimination, brownfields remediation and historical archaeology. Further development and improvements are necessary to expand the applicability of the code. These include the development of a better solver, preconditioner or both. Stable Hankel transform solutions for far field (greater than two skin depths) would improve code performance for calculation of fields at electrically large offsets and for electrically large computational domains.

## REFERENCES

Aruliah, D.A., U.M. Ascher, E. Haber, and D.W. Oldenburg, 1999, A method for the forward modeling of 3D electromagnetic quasi–static problems: M3AS **11**. 1 – 21.

Alexander, C.K., and M.N.O Sadiku, 2004, Fundamentals of Electric Circuits: 2nd edition, McGraw Hill.

Annan, A.P., 1974, The equivalent source method in geophysics: PhD. thesis, Memorial University of Newfoundland.

Badea, E.A., M.E. Everett, G.A. Newman, and O. Biro, 2001, Finite–element analysis of controlled–source electromagnetic induction using Coulomb–gauged potentials: Geophysics, **66**, 786–799.

Barrows, L. and J.E., Rocchio, 1990, Magnetic surveying for buried metallic objects: Ground Water Monitoring Review, **10**, 204–211.

Batayneh, A.T., 2001, Horizontal–loop electromagnetic signature of a buried dike, Al Quweira area, southwest Jordan: Geophysical Prospecting, **49**, 540–546.

Berry, M.W., 1992, Large–scale sparse singular value computations: International Journal of Supercomputer Applications and High Performance Computing, **6**, 13–49.

Biro, O., 1999, Edge element formulations of eddy current problems: Computer Methods in Applied Mechanics and Engineering, **169**, 391–405.

Biro, O., and K. Preis, 1989, Finite element analysis of 3–D eddy currents: IEEE Transactions on Magnetics, **25**, 3145–3159.

Buselli, C., C. Barbar, G. Davies, and R. Salama, 1990, Detection of groundwater contamination near waste disposal sites with transient electromagnetic and electrical methods, *in* Stanley Ward, ed. Geotechnical and Environmental Geophysics: Society of Exploration Geophysics, 27–41.

Canann, S., S. Saigal, and S.E. Owen, 2000, Unstructured mesh generation: International Journal for Numerical Methods in Engineering, **49,** 1–351.

Coggon, J.H., 1971, Electromagnetic and electrical modeling by the finite–element method: Geophysics, **36**, 132–155.

Constable, S., 2006, Marine electromagnetic methods – A new tool for offshore exploration: The Leading Edge, **25**, 438–444.

Davidson, D. B., 2000, Implementation issues for three dimensional vector FEM programs: IEEE Antennas and Propagation Magazine, **42**, 100–107.

Dibben, D.C., and R. Metaxas, 1997, A comparison of errors obtained with whitney and linear edge elements: IEEE Transactions on Magnetics, **33**, 1524–1527

Edwards, R.N., P.A.Wolfgram, and A.S. Judge, 1988, The ICE–MOSES experiment, mapping permafrost zones electrically beneath the Beaufort Sea: Marine Geophysical Research, **9**, 265–290.

Eskola, L., R. Puranen, and H. Soininen,1999, Measurement of magnetic properties of steel sheets: Geophysical Prospecting, **47**, 593–602.

Everett, M.E., and R.N. Edwards, 1993, Transient marine electromagnetics: The 2.5–D forward problem: Geophysical Journal International, **113**, 545–561.

Everett, M.E., and Z. Martinec, 2003, Spatiotemporal response of a conducting sphere under simulated geomagnetic storm: Physics of the Earth and Planetary Interior, **138**, 163–181.

Everett, M.E., and M. A. Meju, 2005, Near–surface controlled–source electromagnetic induction : Background and Recent Advances, *in* Y. Rubin and S. Hubbard, eds., Hydrogeophysics: Kluwer Academy, Chapter **6**, 157–184.

Everett, M.E., and A.Schultz, 1996, Geomagnetic induction in a heterogeneous sphere: azimuthally symmetric test computations and the response of an undulating 660–Km discontinuity: Journal of Geophysical Research, **101**, 2765–2783.

Faires, J.D., and R. Burden, 1998, Numerical Methods: 2nd edition, Brooks/Cole Publishing Company.

Farquharson, C.G., D.W. Oldenburg, and P.S. Routh, 2003, Simultaneous 1–D inversion of loop – loop electromagnetic data for magnetic susceptibility and electrical conductivity: Geophysics, **68**, 1857–1869.

Fernandes, R., 2008, The effects of cultural noise on controlled source electromagnetic responses of subsurface fractures in resistive terrain: M.S. thesis, Texas A&M University.

Freund, R. W., G.H. Golub, and N.M. Nachtigal, 1992, Iterative solutions of linear systems: *in* A. Iserles, ed., Acta Numerica: Cambridge University Press, 57–100.

Geng, N., C.E. Baum, and L. Carin, 1999, On the low frequency natural response of conducting and permeable targets: IEEE Transactions on Geosciences and Remote Sensing, **37**, 347–359.

Grant, F.S., and G.F. West, 1965, Interpretation Theory in Applied Geophysics: McGraw–Hill.

Guptasarma D., and B. Singh, 1997, New digital linear filters for Hankel $J_0$ and $J_1$ transforms: Geophysical Prospecting, **45**, 745–762.

Habashy, T.M., R.W. Groom, and B. Spies, 1993, Beyond the Born and Rytov approximations: A nonlinear approach to electromagnetic scattering: Journal of Geophysical Research, **98**, 1759–1775.

Hoekstra, P., and M. Blohm, 1990, Case histories of time–domain electromagnetic soundings in environmental geophysics, *in* Stanley Ward, ed., Geotechnical and Environmental Geophysics: Society of Exploration Geophysics, 1–15.

Hohmann, G.W., 1987, Numerical modeling for electromagnetic methods of geophysics: v1, *in* M.N. Nabighian, ed., Investigations in Geophysics, no. 3: Society of Exploration Geophysics, 313–366.

Hursan, G., and M. S. Zhdanov, 2002, Contraction integral equation method in 3-D electromagnetic modeling: Radio Science, **6**, 1089.

Jackson, J.D., 1975, Classical Electrodynamics: 2nd edition, Wiley Eastern.

Jin, J. 2002, The Finite Element Method in Electromagnetics: J.W. Wiley and Sons.

Junge, A., 1996, Characterization of and correction for cultural noise: Surveys in Geophysics, **17**, 361–391.

La Brecque, D.J., 1995, A scalar–vector potential solution in finite difference modeling: *in* M. Oristaglio, and B. Spies, eds., International Symposium on Three Dimensional Electromagnetics: Schlumberger–Doll Research, 143–149.

Lamontagne, Y., and G.F. West, 1971, EM response of a rectangular thin plate: Geophysics, **36**, 1204–1222.

Larsson, J., 2007, Electromagnetics from a quasistatic persepective: American Journal of Physics, **75**, 230–239.

Lee, K.H., D.F. Pridmore, and H.F. Morrison,1981, A hybrid three–dimensional electromagnetic modeling scheme: Geophysics, **46**, 796–805.

Levin, D.,1996, Fast integration of rapidly oscillatory functions: Journal of Computational and Applied Mathematics, **67,** 95–101.

Liu, A., and B. Joe,1996, Quality local refinement of tetrahedral meshes based on 8 – subtetrahedron subdivision: Mathematics of Computation, **65**, 1183–1200.

Nabighian, M., 1971, Quasi–static transient response of a conducting permeable two–layer sphere in a dipolar field: Geophysics, **36**, 25 – 37.

Newman, G.A., and D.A. Alumbaugh, 1995, Frequency–domain modeling of air–borne electromagnetic responses using staggered finite differences: Geophysical Prospecting, **43**, 1021–1042.

Palacky, G.J., 1988, Resistivity characteristic of geologic targets: Electromagnetic Methods in Applied Geophysics, *in* Misac N. Nabighian ed., Investigations in Geophysics, No. 3: SEG publications, Chapter **3**, 131–312.

Pasion, L., 2007, Inversion of time domain Electromagnetic data for the detection of unexploded ordnance: PhD. Thesis, University of British Columbia, Vancouver.

Pavlov, D.A. and M.S. Zhdanov, 2001, Analysis and interpretation of anomalous conductivity and magnetic permeability in time domain electromagnetic data Part I: Numerical modeling, Journal of Applied Geophysics, **46**, 217–233.

Price, A.T., 1949, The induction of electric currents in non uniform thin sheets and shells: Quarterly Journal of Mechanics and Applied Mathematics **2**, 283–310.

Qian, W. and D.E. Boerner, 1994, Electromagnetic response of a discretely grounded circuit – An integral equation solution : Geophysics, **59**, 1680–1694.

Rai, S.S., and S.K.Verma, 1982, Quantitative interpretation of horizontal loop EM measurements using the permeable sphere model: Geophysical Prospecting, **30**, 486–500.

Raiche, A.P., and J.H. Coggon,1974, Analytic Green's Tensors for integral equation modeling: Geophysical Journal of the Royal Astronomical Society, **36**, 363–376.

Raiche, A., F. Sugeng, and H. Soinien, 2003, Using the Loki 3D edge finite–element program to model EM dipole–dipole drill–hole data: 16th Geophysical Conference and Exhibition, ASEG Expanded Abstracts.

Ryu, J., H.F. Morrison, and S.H. Ward, 1970, Electromagnetic fields about a loop source of current: Geophysics, **35**, 862–896.

Senos Matias, M., M. Marques da Silva, P. Ferreira, and E. Ramalho,1994, A geological and hydrogeological study of aquifer contaminaton by a landfill: Journal of Applied Geophysics, **32**, 155–162.

Silvester, P.P., and R.L. Ferrari,1996, Finite element methods for electrical engineers: Cambridge University Press.

Song, Y., and J. Kim, 2009, An efficient 2.5–D inversion of loop–loop electromagnetic data: Exploration Geophysics, **39**, 68–77.

Stalnaker, J.L., 2004, A finite element approach to the 3D CSEM modeling problem and applications to the study of the effect of target interaction and topography: PhD. Dissertation, Texas A&M University.

Stalnaker, J.L., M.E. Everett, A. Benavides, C.J. Pierce, 2006, Mutual Induction and the effect of host conductivity on the EM induction response of buried plate targets using 3D finite–element analysis: IEEE Transactions on Geoscience and Remote Sensing, **44**, 251–259.

Sugeng, F., 1998, Modeling the 3D TDEM response using the 3D full–domain finite–element method based on the hexahedral edge–element technique: Exploration Geophysics, **29**, 615–619.

Sugeng, F. and A. Raiche, 2004, Modeling the electromagnetic response in complex geologic structures using the 3D finite–element method based on the hexahedral and tetrahedral edge element technique: 17th Geophysical Conference and Exhibition, ASEG Expanded Abstracts.

Szarka, L., 1988, Geophysical aspects of man–made electromagnetic noise in the earth – a review: Surveys in Geophysics, **9**, 287–318.

Unsworth, M.J., B.J. Travis, and A.D. Chave, 1993, Electromagnetic induction by a finite electric dipole over a 2–D earth: Geophysics, **58**, 198–214.

Ulaby, F. T., 2004, Fundamentals of applied electromagnetics: Pearson Prentice Hall, 2004 media edition.

Velimsky, J., 2003, Electromagnetic induction in a heterogeneous earth's mantle: time domain modeling: PhD. Dissertation, Charles University, Prague, Czech Republic.

Vollaire, C., F. Musy, and R. Perrussel, 2005, Post processing for vector finite element method: from edge to nodal values: COMPEL: International Journal of Computation and Mathematics in Electrical and Electronic Engineering, **24**, 1274–1283.

Wait, J.R., 1982, Geo–electromagnetism: Academic Press.

Wait, J.R., 1955, Mutual electromagnetic coupling of loops over a homogeneous ground: Geophysics, **20**, 630–637.

Walker, P.W., and G.F. West, 1991, A robust integral equation for electromagnetic scattering by a thin plate in conductive media: Geophysics, **56**, 1140–1152.

Walker, P.W., and G.F. West, 1992, Parametric estimators for current excitation on a thin plate: Geophysics, **57**, 766 –773.

Ward, F.S., and G.W. Hohmann,1988, Electromagnetic theory for geophysical applications: Electromagnetic Methods in Applied Geophysics, *in* Misac N. Nabighian ed., Investigations in Geophysics, No. 3: SEG publications, Chapter **4**, 131–312.

Weiss, C.J., and G.A. Newman, 2002, Electromagnetic induction in a fully 3D anisotropic Earth: Geophysics, **67**, 1104–1114.

Xiong, Z., 1992, EM modeling of 3D structures by the method of system iterations using integral equations: Geophysics, **57**, 1556 –1561.

Xiong, Z. and A.C. Tripp, 1995, A block iterative algorithm for 3D electromagnetic modeling using integral equations with symmetrized substructures: Geophysics, **60**, 291–295.

Zhdanov, M.S., and S. Fang, 1997, Quasi–linear series in three dimensional electromagnetic modeling: Radio Science, **32**, 2167–2188.

Zhdanov, M.S., and E. Tartaras, 2002, Three dimensional inversion of multitransmitter electromagnetic data based on the localized quasi–linear approximation: Geophysical Journal International, **148**, 506–519.

Zorin, D., 2006, Subdivision on arbitrary meshes: algorithms and theory: Institute of Mathematical Sciences (Singapore) Lecture Notes Series.

Zunoubi, M.R., J. M. Jin, K.C. Donepudi, and W.C. Chew, 1999, Solving 3–D low frequency electromagnetic diffusion by the finite–element method: IEEE Transactions on Antenna and Propagation, **47**, 242–248.

# VITA

Souvik Mukherjee

Shell Exploration and Production

150 N. Dairy Ashford Road

Houston, TX 77079

*email:* souvikmeister@gmail.com

## EDUCATION

Ph.D. Geophysics, Texas A&M University, College Station, TX, 2010.

M.S. Geophysics, University of Utah, Salt Lake City. UT, 2004.

M.Tech, Appl. Geology, Indian Institute of Technology, Kharagpur, India, 2000.

MSc. Appl.Geology, Jadavpur University, Calcutta, India, 1998.

BSc.Geology with minors in Maths and Physics, Calcutta University 1996.